SPE-193867-MS

Tight Oil and Shale Gas PVT Modelling for Flow Simulation with Matrix-Fracture Interaction

Nicolas Sobecki, IFPEN; Shihao Wang, Colorado School of Mines; Didier-Yu Ding and Carlos Nieto Draghi, IFPEN; Yu-Shu Wu, Colorado School of Mines

This paper was prepared for presentation at the SPE Reservoir Simulation Conference held in Galveston, Texas, USA, 10–11 April 2019.

Abstract

Tight oil and shale gas reservoirs have a significant part of their pore volume occupied by micro (below 2nm) and mesopores (between 2 and 50nm). This kind of environment creates strong interactions forces in the confined fluid with pore walls as well as between its own molecules and then changes dramatically the fluid phase behavior and its thermodynamic properties. Pressure-Vapor-Temperature (*PVT*) modeling of such fluids becomes therefore a challenge in order to get accurate production forecast reservoir simulations. Furthermore along the flow from the matrix to the well through the fractures, the fluid will pass through a very heterogeneous pore size distribution which will alter it differently according to the pore size and the spatial distribution. An important work has therefore to be done on developing upscaling methodology of the pore size distribution for large scale reservoir simulations. Firstly molecular simulations will be performed on pure components and mixtures in order to get reference thermodynamic properties at liquid/vapor equilibrium for different pore sizes. The comparison with commonly used modified equation of state (*EOS*) in the literature highlighted the model of flash with capillary pressure and critical temperature and pressure shift as the best one to match reference molecular simulation results. Secondly fine grid matrix/fracture simulations have been built and performed for different pore size distributions. The study has shown that the pore size distribution has an important impact on reservoir production and that this impact is highly dependent of the volume fraction of nanopores inside the matrix. Capillary pressure heterogeneity and pore radius dependent *EOS* cause gas flow slowdown or gas trapping inside the matrix and postponed gas flow apparition in the fractures during depletion which reduce the *GOR* (Gas-Oil Ratio) at the well. Coarse grid upscaling models have then been performed on the same synthetic case and compared to the reference fine grid results. The commonly used upscaling methodology of dual porosity model with average pore radius for the pore size distribution is unable to match the fine grid results. A new triple porosity model considering fracture, small pores and large pores with their own capillary pressure and *EOS*, together with *MINC* (Multiple Interacting Continua) approach, has shown very good match with the reference fine grid results. Finally a large scale stimulated reservoir volume with different pore size distribution inside the matrix has been built using the upscaling method developed here. The proposed triple porosity methodology

is able to model the PVT of the confined fluid and its flow across a very heterogeneous pore size distribution up to the well through fractures in a large scale reservoir simulation.

Introduction

World energy demand is projected to increase by 30% in 2035 (BP 2017). According to predictions, Fossil fuel will still represent more than three-quarters of world energy consumption through 2040 (U.S. Energy Information Administration 2017). Among oil and gas production, unconventional resources such as shale gas and tight oil have emerged in the past decade as a significant solution for the petroleum industry to meet future world energy demand. Indeed they will reach together nearly thirty percent of global liquids supply by 2040 (ExxonMobil 2018). Tight oil production will more than double from 2015 to 2040 (U.S. Energy Information Administration 2016) and shale production will account for around sixty percent of the increase in gas supplies to 2035 according to (BP 2017).

The flow dynamics and the fluid behavior in shale gas and tight oil reservoirs are much more complex than those in conventional reservoirs. The stimulation of the matrix by multi stage hydraulic fracturing generates a highly heterogeneous porous/fractured rock where flow occurs between an extremely low permeability matrix with nanopores and the fracture up to the well. The modeling of the matrix/fracture exchange in such reservoirs becomes therefore a challenge in terms of flow and phase behavior. An accurate modeling is therefore crucial for optimal production forecasts, which are currently very challenging especially for the Gas-Oil-Ratio (*GOR*) prediction (Kumar et al. 2013; Nojabaei et al. 2013; Tian et al. 2013). Thus this work is aimed to model thermodynamic behavior of a confined fluid inside nanometric pores using molecular simulation as reference for the calibration of a modified Equation of State (*EOS*). This new pore radius dependent *EOS* will then be used in a triple porosity model to take into account the pore size distribution for reservoir simulations.

Tight oil and shale gas reservoirs consist of a very heterogeneous pore size distribution ranging from several nanometers to micro meters contrary to conventional reservoirs where pore size distribution has a micrometer scale. The part of micropores (below 2nm) and mesopores (between 2 and 50 nm) can reach more than 20% of the volume distribution (Kuila and Prasad 2011). They are mainly associated with clay minerals and kerogen (Pommer 2014). Hydrocarbon molecules range between 0.5 and 10 nm (Nelson 2009), then interaction forces between confined fluid and pore wall molecules can become as significant as inter molecular interactions within the confined fluid. Therefore confinement changes dramatically the fluid phase behavior. Several approaches have been used to study the confinement effect in the phase behavior of confined fluids.

Firstly some nanofluidic experiments are showing that the bubble point temperature is increased in nano-channels compared to bulk (Wang et al. 2014; Alfi et al. 2016). Luo et al. (2016) and Cho et al. (2017) conducted the same kind of experiments on pore glasses and mesoporous materials respectively and measured also an increase of bubble point temperature compared to bulk.

Secondly a great deal of work has been done on extension of *EOS* for confined fluid behavior modelling. The modification of the thermodynamic flash by including the capillary pressure represents the first main method used in the literature (Firincioglu et al. 2012; Alharthy et al. 2013; Teklu et al. 2014; Rezaveisi et al. 2015; Xiong et al. 2015; Sandoval et al. 2016; Stimpson and Barrufet 2016; Zhang et al. 2016; Haider and Aziz 2017; Lopez Jimenez et al. 2018). This method is improved by some authors by considering the thickness of the adsorbed layer (Dong et al. 2012; Liu et al. 2016). The second main method used in the literature considers a shift of critical temperature and pressure proportional of pore radius in the flash calculation (Devegowda et al. 2012; Dong et al. 2012; Alharthy et al. 2013; Jin et al. 2013; Sanaei et al. 2014; Teklu et al. 2014; Haider and Aziz 2017; Lopez Jimenez et al. 2018). The correlations used for critical temperature and pressure values versus pore radius are either analytical (Meyra et al. 2005) or build from molecular simulation results (Jin et al. 2013; Sanaei et al. 2014). The two methods of capillary pressure

consideration and shift of critical properties are also applied together (Teklu et al. 2014; Dong et al. 2016; Lopez Jimenez et al. 2018; Zuo et al. 2018). The pore/fluid interaction effect has also been included by some authors to build a new *EOS*. Interaction parameters must be fitted with experimental or molecular simulation results (Travalloni et al. 2010; Travalloni et al. 2014; Barbosa et al. 2016; Islam and Sun 2016).

Finally molecular simulation appears to be the best way to approach the reality of the thermophysics of confined fluids. Pitakbunkate et al. (2016; 2017) have applied Grand Canonical Monte Carlo ensemble (*GCMC*) to methane/ethane mixture phase behavior calculation. Jin et al. (2017) modified the *GCMC* ensemble to create the gauge-*GCMC* method and studied pure system, binary and ternary system. The Gibbs Ensemble Monte Carlo (*GEMC*) developed by Panagiotopoulos (1986) and improved by Panagiotopoulos (1987) has been widely used for confined pure fluid equilibria (Panagiotopoulos 1987; Shaoyi and Keith E. 1995; Gelb et al. 1999; Rahmani Didar and Akkutlu 2015) but very few work have been done for mixtures (Rahmani Didar and Akkutlu 2015). Other authors are using Grand Canonical Transition Matrix Monte Carlo (Siderius and Gelb 2011) and Configurational-biais grand-canonical transition-matrix Monte Carlo simulations (Singh et al. 2009; Singh and Singh 2011) for confined fluid properties calculations. Whatever the ensemble used, the observations are the same for all authors cited above. The confinement causes a shift of critical temperature and pressure of the fluid from their bulk value and vapor density increases while liquid density decreases. These observations are independent of pore shape and composition (Singh and Singh 2011; Jin and Nasrabadi 2018) and pore size distribution (Jin et al. 2017).

All the methods cited above aim to model the confined fluid *PVT* for a given pore radius. The study of the impact of fluid confinement on reservoir production has been carried out by several authors for a constant pore radius value. Firincioglu et al. (2012), Nojabaei et al. (2014), Xiong et al. (2015) and Haider and Aziz (2017) ran reservoir simulations with capillary pressure effect on the phase behavior. They all studied oil system and showed that oil production is increased and gas production is decreased. Devegowda et al. 2012, Alharthy et al. 2013, Sanaei et al. 2014, Haider and Aziz 2017 and Lopez Jimenez et al. 2018 ran reservoir simulations with critical properties shift effect on the phase behavior and showed that oil and gas production is increased regardless of fluid type.

However the pore network is in reality very complex and the reservoir has an important heterogeneity of pore sizes. Upscaling methodologies must therefore be developed in order to perform large scale reservoir simulations. Few authors have applied the pore size distribution in their model and most of them have considered an average pore radius inside a simulation cell (Firincioglu et al. 2013, Sanaei et al. 2014, Alharthy et al. 2017, Haider and Aziz 2017 and Lopez Jimenez et al. 2018). Alharthy et al. (2017) used a double porosity model with three facies in the matrix subgrid corresponding to a given critical point shift, permeability and flow capillary pressure. Firincioglu et al. (2013) used a black oil single porosity model with a random distribution of capillary pressure in the grid. The value of the bubble point in each cell is suppressed by the value of the capillary pressure inside the cell plus the excess suppression calculated from a correlation. Sanaei et al. (2014) used a single porosity model with critical shift method and ran reservoir simulations on a random pore size per cell according to a given distribution. Lopez Jimenez et al. (2018) did the same work and used the flash with capillary pressure. Haider and Aziz (2017) ran numerical simulations for two different pore size distributions using a fixed pore radius per cell for flash computation with capillary pressure or critical point shifts, and concluded that oil production is increased when the percentage of cells of small pore radius is high. Others authors considered the pore size distribution using the J Leverett functions or an effective radius function of the saturation of the wetting fluid. Li et al. (2016) and Li and Mezzatesta (2017) considered a radius function of saturation in the Laplace equation of the flash. This effective radius is built from a volumetric pore size distribution. They generated black oil properties but did not perform reservoir simulations. Nojabaei et al. (2014) developed a method called "compositionally-extended Black Oil formulation". Black oil properties are firstly generated by a flash with capillary pressure for different pore radius. A K-value compositional reservoir simulation is then run for saturation calculation.

This saturation gives the effective radius thanks to the Laplace equation. Wang et al. (2013) and Xiong et al. (2015) used a single porosity model with flash with capillary pressure calculated by the J Leverett function at specific saturation. These two methods are quite similar and seem not to be efficient. As the percentage of micro and meso pores inside shale matrix is low, the effective radius value stays quite high (or low J Leverett function value) for a large range of wetting phase saturation during the flow simulation. Then the impact of confinement is very low and the fluid behaves like bulk. Alfi et al. (2017) proposed a triple porosity method with three permeability, three porosity model to account for filtration effect in shale reservoirs. The porous media is divided into three different sub-media: fracture, large pores and small pores. Peng-Robinson *EOS* is used for flash calculation in large pores and fractures and a modified Peng-Robinson equation of state (Travalloni et al. 2014) is used for small pores for a specific radius in order to account for confinement effect. The two *EOS* must be solved simultaneously. All fugacities must be equal at equilibrium in both phases for the both sub media (large and small pores) for every component. This method is interesting but seems to be very time consuming and no clear details are given on the thermodynamic equilibrium calculation and how to model the flux between sub-grids. Besides, we are not sure if the thermodynamic equilibrium between small and large pores is predominant comparing to other effects such as capillarity during a dynamic flow simulation.

To our knowledge, the two main methods to model confined fluid *PVT* behavior, that is, flash with capillary pressure and flash with critical point shift, have not been compared to reference data. Using molecular simulation seems to be a best way to approach reality and to construct reference data. In this paper, a robust and innovative molecular simulation workflow aiming to get thermodynamic properties of pure components and mixtures in confined space will be presented (Sobecki et al. 2019). A comparison of these data with modified *EOS* will also be performed. In the literature, the confinement effect on reservoir production has been mainly studied with a single pore size model in large simulation cells, but the impact of pore size distribution inside a simulation cell, especially in the scale of matrix-fracture transfer, has been poorly considered. In the second part of this paper, we present the study of the pore size distribution on the matrix-fracture transfer problem using fine grid simulations. Then, an upscaling methodology of the pore size distribution will be investigated on a coarse grid model for matrix-fracture exchange simulations. A new triple-porosity model together with a *MINC* approach will be proposed and a large scale reservoir simulation will be presented.

Molecular simulation and PVT modeling

Molecular simulation

Workflow. In molecular simulation, Monte Carlos method aims to generate in a given statistical ensemble a collection of configurations (spatial coordinates of molecules) representative of the system at equilibrium. In this collection, each configuration must satisfy the probability density of the given statistical ensemble. It is like a sampling of molecules positions at equilibrium for a specific statistical ensemble. Thermodynamic properties of the fluid can therefore be calculated as the average of the macroscopic properties over the number of configurations.

Molecular simulations have been applied to a hydrocarbon fluid confined in a nanometric pore. The case of study is a slit pore with graphite walls, which is a simplified model of kerogen pores present in tight oil and shale gas reservoirs. Two infinite parallel slices are in the directions orthogonal to the slit pore (i.e. x and y) and the slit pore has a width of length H in the direction z.

As an extension to the work of Jiang and Gubbins (1995) from two dimensions to three dimensions, the confined Gibbs Ensemble Monte Carlo (*GEMC*) *NVT* method (Figure 1) will be used to get thermodynamic properties of the confined fluid. This method gives accurate results for liquid-vapor equilibrium as it considers one liquid simulation box and one vapor simulation box in thermodynamic equilibrium. However

it needs good initial conditions to converge. The Grand Canonical Monte Carlo ensemble (*GCMC*) simulation results will be used as initialization for pure fluids and a new method called *NPT-BPMC* developed by Sobecki et al. (2019) will be used for mixtures. A description of the *GCMC* methods is given in Appendix A. The *NPT-BPMC* method is a new ensemble based on the classic Gibbs *NPT* version (Panagiotopoulos et al. 1987) with Bubble Point Monte Carlo which is a bubble point pseudo-ensemble suggested by (Ungerer et al. 1999) and improved by (Ferrando et al. 2010) for liquid mixture bubble pressure calculation. Sobecki et al. (2019) has adapted this method for confined fluid mixture thermodynamic equilibrium property calculation. The Gibbs code from IFPEN and the LCP laboratory at university Paris XI is used for all the simulations (Ungerer et al. 2005).

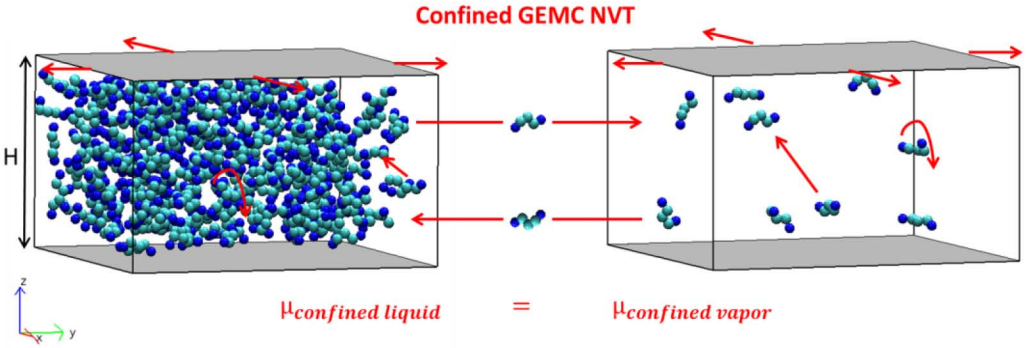

Figure 1—Schematic of the GEMC *NVT* method, example of n-pentane. Figure from Sobecki et al. (2019)

In the Gibbs *NVT* ensemble, the number of particles N, the total volume V and the temperature T are constant. The two phases are represented by two boxes of total volume V with N particles in total. During the simulation, different trial moves are randomly proposed and accepted according to the probability acceptation. The moves are translation and rotation of a particle inside a box, transfer of a randomly selected particle from one box to the other and change of volume in such a way that the total volume remains constant. In our case of confinement of a slit pore of width H, modifications have been done to allow volume changes only in the directions orthogonal to the slit pore (i.e. x and y). Simulations for longer chain molecules such as n-pentane and n-decane have internal translation and rotation in addition. After several Monte Carlo steps, the thermodynamic average of macroscopic properties can be calculated on stabilized configurations to give the properties at liquid/vapor equilibrium. More details about the *GEMC NVT* simulation can be found in (Daan Frenkel and Berend Smit 1996).

Force field. Three interaction types are taken into account: fluid-fluid interaction, solid-fluid interaction and solid-solid interaction. The Steele potential (Steele 1973; Gelb et al. 1999) models the fluid-solid interactions and the solid-solid interactions are fully neglected. This potential considers only the first layer of the graphite pore wall, the remaining layers are considered as continuum solid (Siderius and Gelb 2011).

The Steele 9-3 potential is used in the simulation:

$$u_{sf}(r_{sf}) = \frac{2}{3}\pi\rho_s\varepsilon_{sf}\sigma_{sf}^3\left(\frac{2}{15}\left(\frac{\sigma_{sf}}{r_{sf}}\right)^9 - \left(\frac{\sigma_{sf}}{r_{sf}}\right)^3\right) \quad (1)$$

where r_{sf} corresponds to the distance between solid and fluid particles and ρ_s is the atomic density of solid. σ represents the distance between two atoms where attractive and repulsive forces are canceled and ε is energy and represents the depth of the potential well (at the minimum of the function). The values of these parameters can be found in (Porcheron et al. 1999).

The fluid-fluid interactions are modeled by the Lennard-Jones 12-6 potential:

$$U_{ij}^{LJ}(r_{ij}) = 4\varepsilon_{ij}\left(\left(\frac{\sigma_{ij}}{r_{ij}}\right)^{12} - \left(\frac{\sigma_{ij}}{r_{ij}}\right)^{6}\right) \quad (2)$$

where r_{ij}, ε_{ij} and σ_{ij} are the distance, the *LJ* well depth and the *LJ* diameter respectively.

Lorentz-Berthelot Mixtures laws are used for solid/liquid and liquid/liquid interactions:

$$\sigma_{ij} = \frac{\sigma_{ij} + \sigma_{ij}}{2} \quad (3)$$

$$\varepsilon_{ij} = \sqrt{\varepsilon_{ij}\varepsilon_{ij}} \quad (4)$$

Periodic boundary conditions are applied in all directions for the bulk system and in x and y directions for the confined fluid. The Lennard-Jones interactions are only calculated in a sphere of radius corresponding generally to the half-length of the simulation box because of computational constraint. A long distance correction is therefore applied considering homogeneous density of the environment beyond this radius. Long range correction is not used for the slit pore as there are no periodic boundary conditions in the slit width direction. All studied molecules are described using the *AUA4* (Anisotropic United Atoms model) optimized parameters (Ungerer et al. 2000; Bourasseau et al. 2002). The *AUA* model consists of a displacement of the Lennard Jones centers of force toward the hydrogen atoms. The parameters describing the force field for non-flexible and flexible particles are summarized Table 7 and Table 8 (Porcheron et al. 1999; Ungerer et al. 2000; Bourasseau et al. 2002) in the Appendix A.

Simulation data post-processing

When the stationary state is reached, the number of particles inside the simulation box at each step fluctuates around its average value and then the system is at equilibrium. The average of a macroscopic propriety *X* (energy, density…) is calculated by:

$$< X >= \frac{1}{n}\sum_{i=1}^{n} X(r_i^N) \quad (5)$$

where *n* is the number of configurations and r_i^N the positions of the particles in configuration i (or sampling i).

The density of a component i at equilibrium can be calculated by:

$$\rho_i = \frac{< N_i > M_i}{V_{box} N_{av}} \quad (6)$$

For mixtures, phase densities and molar fractions are calculated by:

$$\rho_l = \frac{\sum_i < N_i^l > M_i}{V_{box} N_{av}} \quad (7)$$

$$\rho_v = \frac{\sum_i < N_i^v > M_i}{V_{box} N_{av}} \quad (8)$$

$$x_i = \frac{< N_i^l >}{\sum_i < N_i^l >} \quad (9)$$

$$y_i = \frac{< N_i^v >}{\sum_i < N_i^v >} \quad (10)$$

where V_{box} is the volume of the box, $<N_i>$ the average number of particles of component i, M_i its molar mass, N_{av} the Avogadro number, the *l* subscription refers to liquid phase and *v* refers to vapor phase.

The critical parameters are estimated with the least square fit of the following scaling law (Vega et al. 1992):

$$\rho_l - \rho_v = B\left(1 - \frac{T}{T_c}\right)^{\beta} \tag{11}$$

where β=0.325 and B is a constant to adjust. The estimated critical temperature is then used to calculate the critical density from the least square fit of the following equation (Lambert J.Van Poolen, Cynthia D.Holcomb, Vicki G.Niesen 1997):

$$\frac{\rho_l - \rho_v}{2} = \rho_c + A(1 - \frac{T}{T_c}) \tag{12}$$

where A is a constant to adjust. Finally the critical pressure is obtained from Antoine equation (equation 13) which is derived from the Clausius Clapeyron equation which results from the fitting of the vapor pressure values obtained at each temperature.

$$\ln(P_c) = C + \frac{D}{T_c} \tag{13}$$

where C and D are constants to adjust. C and D correspond respectively to the intercept and the slope of $ln(P_v)$ versus $1/RT$, where P_v is the vapor pressure and R the ideal gas constant.

Simulation Results

Critical points calculation of pure components has been performed from *NVT* simulation results for different pore lengths (Sobecki et al. 2019). Methane critical point evolution versus pore radius is shown Figure 2 and compared with literature results. The evolution of critical temperature versus pore length differs from the evolution of critical pressure. But both tend towards bulk value at high pore length. The results for critical temperature are close to those from (Singh and Singh 2011; Pitakbunkate et al. 2016) which is not the case for critical pressure because the methods used by the different authors are different. Pitakbunkate et al. (2016) used the pressure of the bulk fluid in equilibrium with the confined fluid and monitored the end of density discontinuity versus pressure. Singh and Singh (2011) calculated a unique saturation pressure from the coexistence probability distribution and applied equation 13 for critical point calculation. The correlation from Jin et al. (2013) is well adapted and matches the results. The analytical solution from Meyra et al. (2005) is more adapted for critical pressure than that of Jin et al. (2013), which leads to negative values for longer chain alkanes.

Sobecki et al. (2019) has performed molecular simulations using *GEMC NPT BPMC* and *GEMC NVT* on two mixtures: methane/ethane and ethane/n-pentane. Examples of pressure versus temperature phase diagram for a specific composition have been built for methane/ethane and ethane/n-pentane. The phase envelop of the confined fluid is shifted inwards and closes itself from its bulk value. So, the critical temperature and pressure are shifted from the bulk value to a lower value, the bubble point is decreased and the dew point is increased with confinement

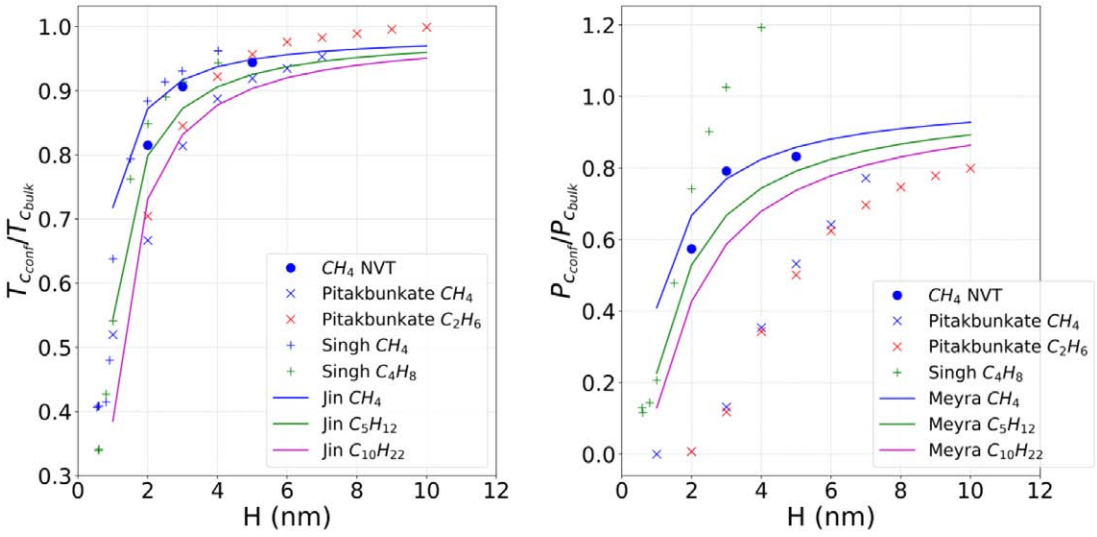

Figure 2—Comparison of critical temperature and pressure evolution with literature (Meyra et al. 2005; Singh and Singh 2011; Jin et al. 2013; Pitakbunkate et al. 2016).

PVT modeling

Modification of the flash. The method used for the implementation of capillary pressure for a fixed radius in the two phase flash was inspired by Shapiro and Stenby (2001), Yi Xiong (2015), Stimpson and Barrufet (2016) and Haider and Aziz (2017). The implemented algorithm is illustrated in Figure 3 and follows the steps below.

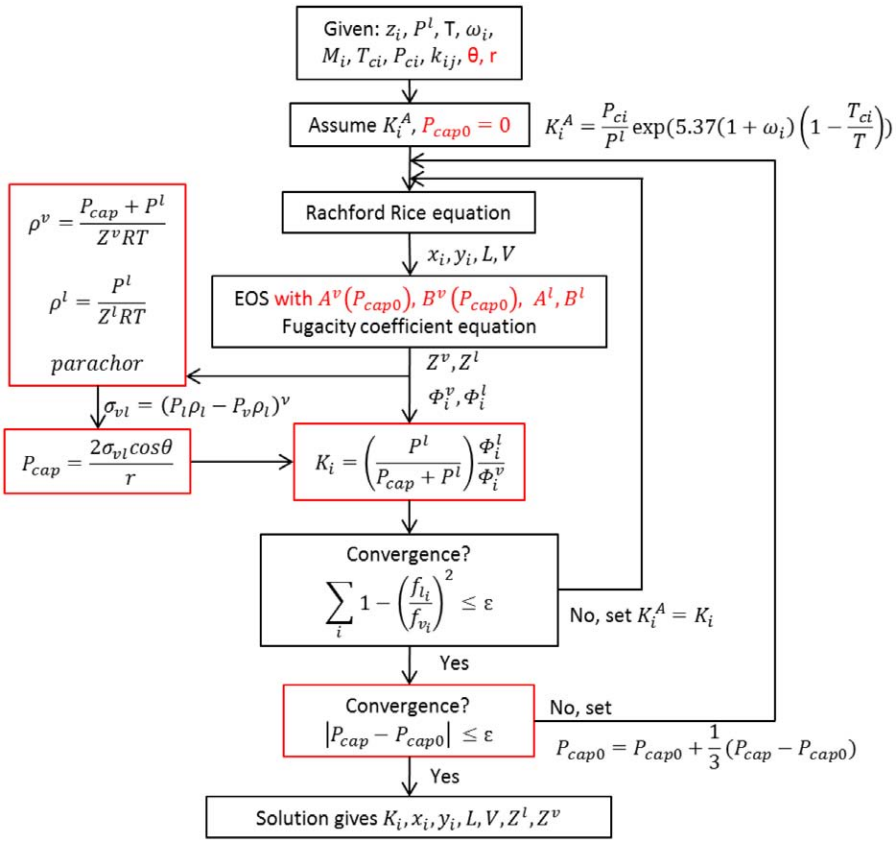

Figure 3—Two phase flash algorithm with capillary pressure.

Step 1: An initial value of K_i is assumed for each component. This starting value comes from the Wilson's equation.

Step 2: The Rachford Rice equation is solved to determine the vapor molar fraction V, which gives the liquid molar fraction with $L=1-V$, and the liquid and vapor molar fraction $x_i = \frac{z_i}{L+VK_i}$, $y_i = \frac{z_i K_i}{L+VK_i}$ for the component i.

Step 3: The *EOS* is solved for liquid and vapor to get Z^l and Z^v. Then the fugacity coefficients Φ_i^l and Φ_i^v are determined using the equations of fugacity coefficient.

Step 4: The interfacial tension (*IFT*) is calculated by the parachor model of Zuo and Stenby (1998).

$$\sigma_{vl} = (P_l\rho_l - P_v\rho_v)^v \tag{14}$$

with

v=3.6

σ_{vl}: interfacial tension (dynes/cm=mN/m)

P_l=$\sum_i x_i P_i$: liquid parachor

P_l=$\sum_i y_i P_i$: vapor parachor

ρ_l : molar density of liquid phase (mole/cc)

ρ_v : molar density of vapor phase (mole/cc)

$P_i = (8.21307 + 1.97473\omega_i)T_{ci}^{1.03406}p_{ci}^{-0.82636}$: parachor of pure component with T_c in K and P_c in bar.

ω_i : acentric factor

Then capillary pressure P_{cap} is calculated by the Laplace equation.

Step 5: The new equilibrium ratio $K_i = y_i/x_i$ is calculated.

Step 6: The convergence of fugacity and capillary pressure is checked. If there is convergence, then the solution has been reached. If not, steps 2 through 5 are repeated with the new *Ki* value. The update of the capillary pressure in the loop follows an under-relaxation scheme in order to avoid convergence issues, especially during reservoir simulations. Indeed the Rachford Rice equation has a physical solution only if there is one of the *Ki* values higher than one (Curtis H.Whitson and Michael L.Michelsen 1989). Considering the formulation of the update of *Ki*, the value of the capillary pressure cannot be too high in an iteration step for the flash calculation. In our algorithm, we increase gradually the capillary pressure by a factor of 1/3 in the iterations.

The Peng-Robinson *EOS* (Peng and Robinson 1976) is used in this algorithm. The contact angle θ is considered to be zero for all the simulations. The flash with critical pressure and temperature shift is performed on a classic flash which is the same flash algorithm explained in Figure 3 but with zero capillary pressure. The critical temperature and pressure input parameters for a given pore radius is calculated using the Jin et al. (2013) correlation and with Meyra et al. (2005) correlation respectively. These correlations have shown a good match with our molecular simulation results (see, Figure 2). Both methods of flash with capillary and shift of critical temperature and pressure can also be used together, although one might wonder the redundancy of this information.

Comparison with molecular simulations. The thermodynamic properties at liquid/vapor equilibrium of confined hydrocarbon mixtures obtained using molecular simulation (Sobecki et al. 2019) are considered as reference data for *EOS* calibration. The effect of confinement on fluid properties can be observed in Figure 4. The vapor density is increasing, the liquid density is decreasing (Figure 4 right). The critical pressure is decreasing with a value bellow the bulk value and the bubble point is decreased whereas the dew point is increased with confinement (Figure 4 left). The three main methods used in the literature such as flash with capillary pressure, flash with shift of critical temperature and pressure and flash with both methods used together have been compared with *NVT* results for methane/ethane in a 3 nm slit pore at 240K (Figure 4).

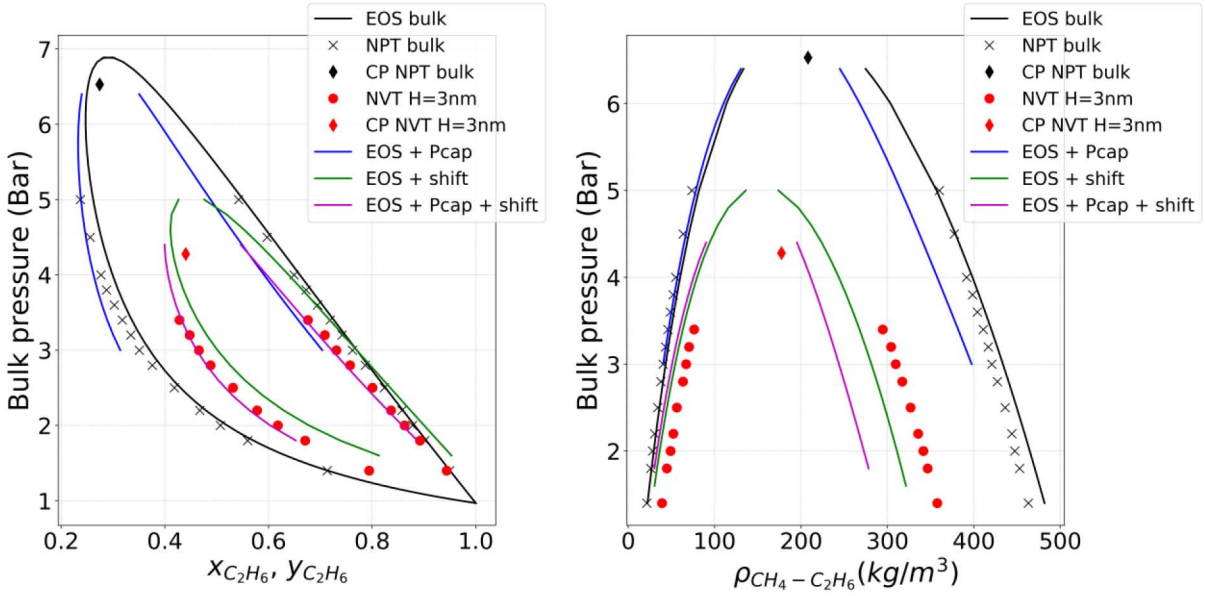

Figure 4—Comparison of *EOS* modifications with molecular simulation results (Sobecki et al. 2019) for methane/ethane mixture at 240K in a 3nm slit pore. *EOS + Pcap* corresponds to a flash with capillary pressure with a 3nm pore length. *EOS + shift* corresponds to a flash with shift of critical pressure and temperature following the Meyra et al. (2005) and Jin et al. (2013) correlation respectively with a 3nm pore length. *EOS + Pcap + shift* corresponds to both methods used at the same time.

For our flash simulations with capillary pressure, as the mixtures are mainly composed of light components, gas pressure is used as reference. For this example the method of flash with capillary pressure and shift of critical properties is the most suitable method for matching the reference molecular simulation data. A volume correction such as Péneloux et al. (1982) which is independent of the flash calculation is needed in order to match well the liquid and vapor densities.

Pore size distribution impact on reservoir production

As shale gas and tight oil reservoirs are usually fractured, and the nanopore physics impact only the fluid flows inside the matrix medium and between the matrix and fracture transfer, we will study the matrix-fracture exchange process in the scale of a matrix block size. The pore size distribution should be considered in this matrix-fracture interaction.

Simulation cases

In order to study the impact of the pore size distribution (*PSD*) on reservoir production, a synthetic reservoir case representing the matrix/fracture interaction has been built with different *PSD*. The synthetic case is a two dimensional single porosity model representing the matrix/fracture exchange. A tight matrix rock of 5m width, 0.5m height and 0.05m thickness is in contact with a fracture of 0.005m width on its right side (Figure 9). Pressure in the fracture is maintained at a constant value of 100 bar and only oil and water are present at the initial condition. The initial pressure is 200 bar and depletion is simulated to model flow from the matrix towards the fracture. Bakken oil (Nojabaei et al. 2013; Xiong et al. 2015) is used for the simulations and the different compositional parameters are given in Table 1 and Table 2. For information, bubble point at the reservoir temperature of 373.15 K is 176.7 bar. All the simulation parameters are summarized in Table 3. In order to get reliable results, the grid is very fine with grid cells of 0.05*0.05*0.05m. The permeability of the matrix has been chosen to be 100 nD in accordance with works from Wang and Reed (2009).

Table 1—Compositional data for Bakken oil

Component	*Molar fraction*	*Critical pressure (MPa)*	*Critical temperature (K)*	*Molar Weight (kg/kgmol)*	*Acentric factor*	*Critical Volume (m3/kgmol)*
C1	0.36736	4.599	190.56	16.04	0.0115	0.0986
C2	0.14885	4.872	305.32	30.07	0.0995	0.1455
C3	0.09334	4.248	369.83	44.10	0.1523	0.2000
C4	0.05751	3.796	425.12	58.12	0.2002	0.2550
C5-C6	0.06406	3.181	486.38	78.30	0.2684	0.3365
C7-C12	0.15854	2.505	585.14	120.56	0.4291	0.5500
C13-C21	0.0733	1.721	740.05	220.72	0.7203	0.9483
C22-C80	0.03707	1.311	1024.72	443.52	1.0159	2.2474

Table 2—Binary interaction parameters for Bakken oil

	C1	***C2***	***C3***	***C4***	***C5-C6***	***C7-C12***	***C13-C21***	***C22-C80***
C1	0	0.005	0.0035	0.0035	0.0037	0.0033	0.0033	0.0033
C2	0.005	0	0.0031	0.0031	0.0031	0.0026	0.0026	0.0026
C3	0.0035	0.0031	0	0	0	0	0	0
C4	0.0035	0.0031	0	0	0	0	0	0
C5-C6	0.0037	0.0031	0	0	0	0	0	0
C7-C12	0.0033	0.0026	0	0	0	0	0	0
C13-C21	0.0033	0.0026	0	0	0	0	0	0
C22-C80	0.0033	0.0026	0	0	0	0	0	0

Table 3—2D simulation parameters

	Matrix	*Fracture*
Number of cells	100*10*1	1*10*1
dx/dy/dz (m)	0.05/0.05/0.05	0.005/0.05/0.05
k(D)	10^{-7}	10
porosity	Facies dependant	1
Initial pressure (bar)	200	
Initial temperature (K)	373.15	
Initial water saturation S_{wi}	0.3	
Fracture pressure (bar)	100	

The matrix *PSD* is divided into three facies corresponding to different ranges of pore size and porosities (Table 4). Facies 1 correspond to the small pores with pore radius ranging from 2 to 10nm, facies 2 corresponds to large pores from 10 to 100nm and facies 3 corresponds to pore radius above 100 nm or bulk, where confinement has no effect on the fluid phase behavior. The *PSD* in each facies is generated by a lognormal distribution with a mean of 3 and a standard deviation of 1 (Figure 6). Five *PSD* are considered in the matrix, and these *PSD* correspond to different fractions of the three facies (Table 5). The distribution D2 corresponds to the study of a typical shale reservoir by Kuila and Prasad (2013) and interpreted by Alharthy et al. (2013).

Table 4—pore size distribution properties

Facies	*Pore size (nm)*	*porosity*
1	2-10	ε_{f1}=0.02
2	10-100	ε_{f2}=0.05
3	> 100	ε_{f3}=0.1

Table 5—Grid volume and pore volume per facies for the different distributions

Distribution	*Grid volume fraction (%)*			*Pore volume fraction (%)*		
	Facies 1 (v_{f1})	**Facies 2 (v_{f2})**	**Facies 3 (v_{f3})**	**Facies 1**	**Facies 2**	**Facies 3**
D1	10	20	70	2.5	12	85.5
D2	19	22	59	5	15	80
D3	20	40	40	6	31	63
D4	25	45	30	9	39	52
D5	35	50	15	15	53	32

Ten realizations for each five PSD are generated. So, in total, fifty realizations are obtained with ten for each of the five distributions D1, D2, D3, D4 and D5. Figure 5 is an example of one of the ten realizations for Distribution D3. Realization examples of *PSD* for each distribution D are given in Appendix B (Figure 22 to Figure 31). It is assumed that the three facies have the same relative permeability but different capillary pressures (Figure 7). Capillary pressure is assigned according to the pore size, the facies three which corresponds to bulk fluid has zero capillary pressure unlike facies one and two (Figure 7).

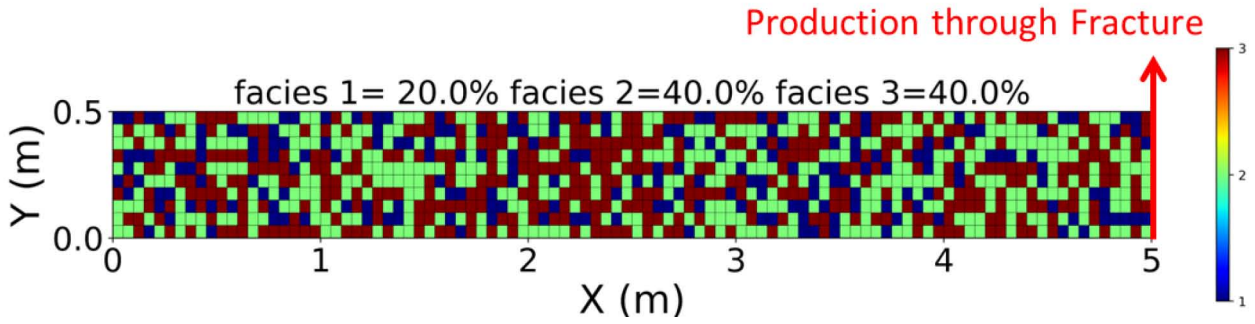

Figure 5—Example of one of the ten facies spatial distribution of D3 in the matrix

Concerning the *PVT* modelling of the fluid, the two commonly used methods of flash with capillary pressure and flash with critical properties shift have been chosen. The flash algorithm illustrated in Figure 6 has been included in an in-house compositional simulator.

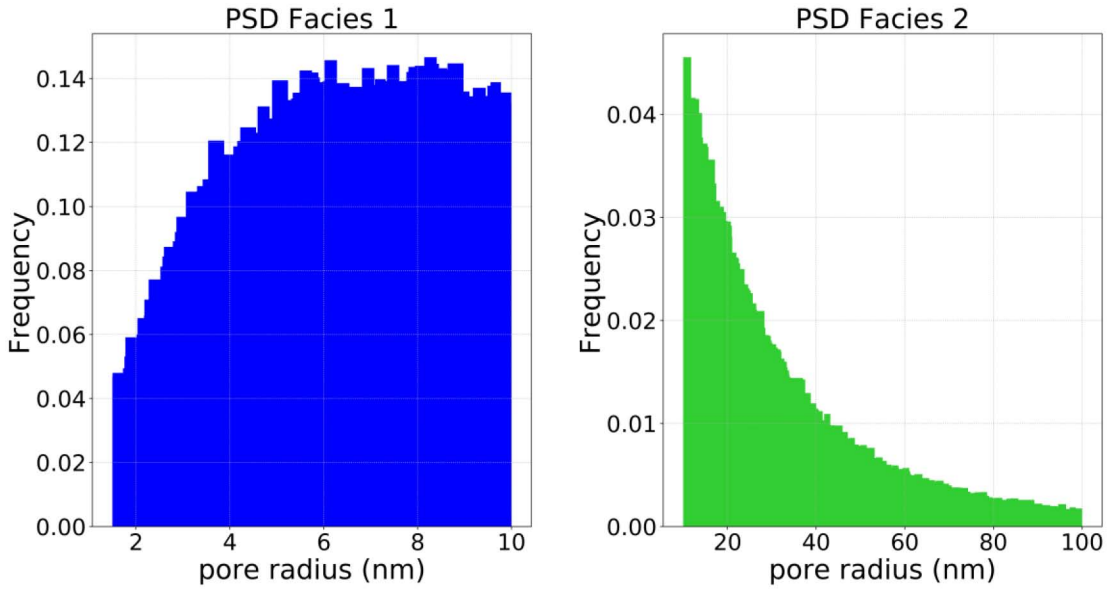

Figure 6—Histogram of an example of a *PSD* sample for facies 1 and 2 using the lognormal law distribution with a mean of 3 and a standart deviation of 1.

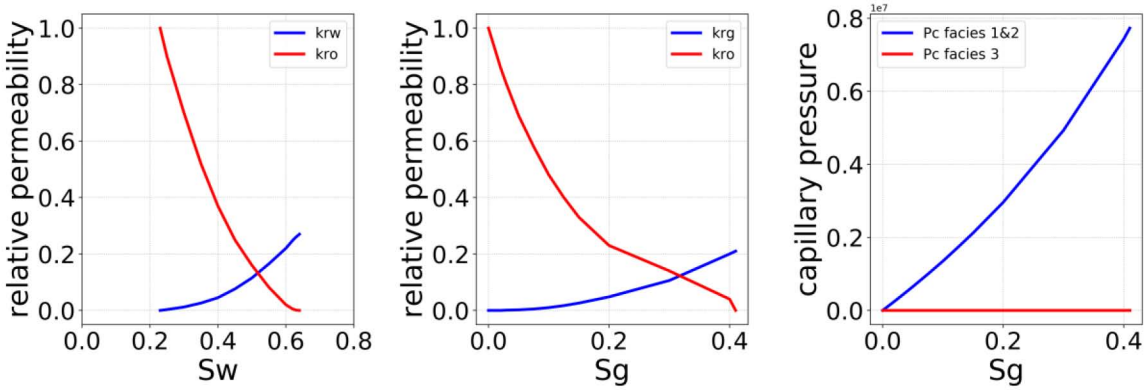

Figure 7—relative permeability and capillary pressure curves

Fine grid simulations

As explained in the previous section, ten simulations corresponding to different realisations have been performed for each distribution D. Figure 32 in Appendix B is an example of the production results for the ten realizations of D1. The results are different for each of the ten realizations because of the difference of spacial capillary pressure heterogeneity and *PVT* behavior due to extremely small pore sizes. In order to compare the different distributions D, the production data of the ten realizations of each D is represented by their average value P50 and their percentiles P10 and P90. We first present the results with flash with capillary pressure used for *PVT* modelling for facies one and two.

The gas and oil recovery factors and the gas-oil ratio (*GOR*) of the different distributions D are compared to same case simulations using bulk fluid, i.e. with zero capillary pressure in the entire matrix and no modification done in the flash. As the porosities are different for each distributions D, the bulk simulation results are also different. The results for the different distribution D are shown Figure 33 to Figure 37. In all cases and compared to bulk fluid, the oil production is increased, the gas production and the *GOR* is decreased with fluid confinement. Two different effects are present and can explain this observation: the capillary pressure heterogeneity and the pore dependent *PVT* modelling. The capillary pressure heterogeneity will slow down the gas flow or even stuck the volume of gas present in facies 3 where capillary pressure is zero. The density of oil will then become lighter and the matrix pressure will be

maintained for a longer time. Therefore gas production will decrease and oil production will increase, the GOR will then decrease. On the other hand the modification of the flash with capillary pressure decreases the bubble point of the oil. Gas apparition is then postponed during depletion and oil stays lighter for a longer time, which leads to the same conclusion for production observations.

The Figure 8 compares the P50 value of reservoir production for the different distributions D. When the percentage of nanopores of facies 1 and 2 increases (i.e. from D1 to D5), the production of oil increases until D4 and then decreases, the production of gas and the GOR decreases until D3 or D4 (they have almost the same P50, especially in the first 10-15 years) and then increases. The capillary pressure heterogeneity has a strong impact on production for low percentage of nanopores in the matrix because large volume of facies 3 might be surrounded by facies 1 and 2 where the capillary pressure is very high, and then important volume of gas stays stuck in facies 3. When the percentage of nanopores becomes important (D4, D5), the volume of facies 3 surrounded by facies 1 and 2 is very small and no gas entrapment occurs. However the volume of cells with lower bubble point due to modified *PVT* modeling becomes significant to impact the production. For the studied cases it seems that the impact on production of capillary pressure heterogeneity is more important than confined fluid PVT behavior. This could explain the trend inversion of the curves from D4 to D5.

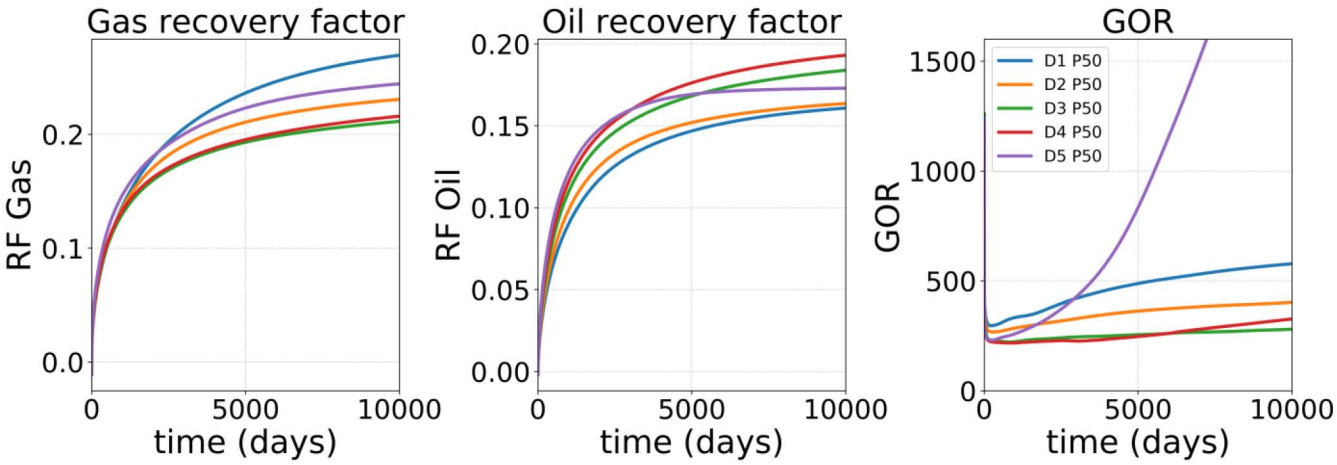

Figure 8—Comparison of production results for the different distributions with a flash with capillary pressure

The impact of pore size dependent *PVT* modeling can be analyzed by comparing reservoir simulation models with capillary pressure heterogeneity and confined fluid *PVT* model and reservoir models with capillary pressure heterogeneity and bulk fluid *PVT*. Figure 9 shows the difference between these two models for d1, one of the ten realizations. The two different models are quite similar from D1 to D3 which mean that modified *PVT* modelling has no strong impact on production for such distributions. However for D4 and especially D5 with higher percentage of nanopores, the difference between the two models is significant which mean that pore radius dependent *EOS* has an important impact on production for these distributions.

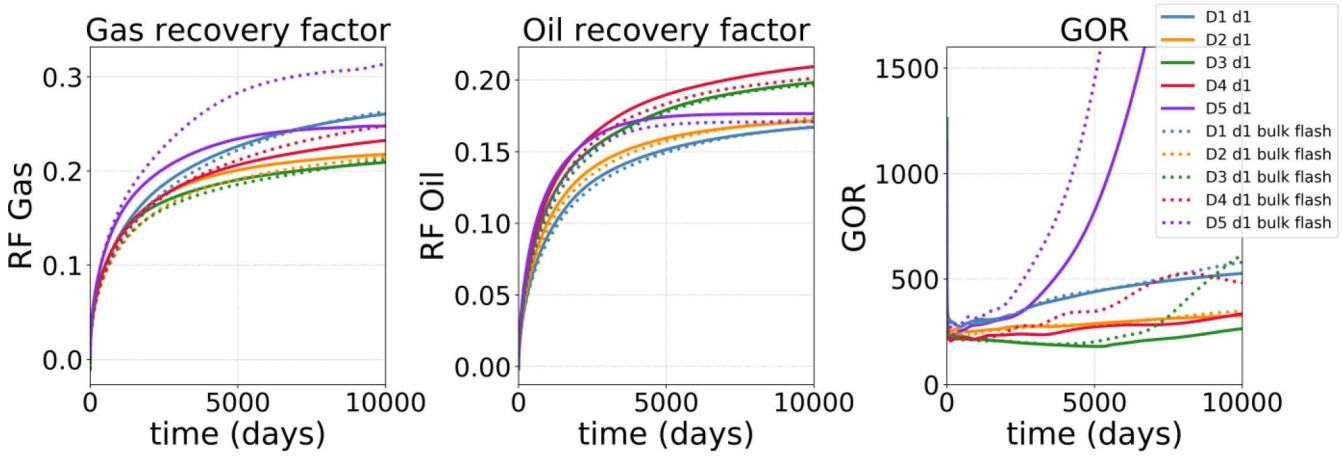

Figure 9—Impact of modified EOS on production

The production results for the five different distributions are now presented with flash with critical pressure and temperature used for *PVT* modelling for facies one and two (see Figure 38 in Appendix B). The conclusions are similar to the case with a flash with capillary pressure. Compared to flash with bulk fluid, the oil production is increased, the gas production and the *GOR* is decreased with fluid confinement. However it is important to note that changing critical pressure and temperature alters the fluid which provides a different initial mass, transport and volumetric properties in the single phase compare to bulk. Concerning the evolution of production against the increase of percentage of nano-pores (from D1 to D5), the observations are also the same. The production of oil increases until D4 and then decreases, the production of gas and the *GOR* decreases until D3 and then increases. The explanations used for the case of flash with capillary pressure are applicable to the case of flash with critical pint shift.

The comparison with previous results obtained using a flash with capillary pressure is showed Figure 10. The results for D1, D2 and D3 are very similar; indeed the small pores have a low percentage, and the impact of modified *PVT* modelling is negligible compare to capillary pressure heterogeneity. However for D4 and D5 with a higher proportion of nanopores, the difference is quite significant because the two modified PVT models are different.

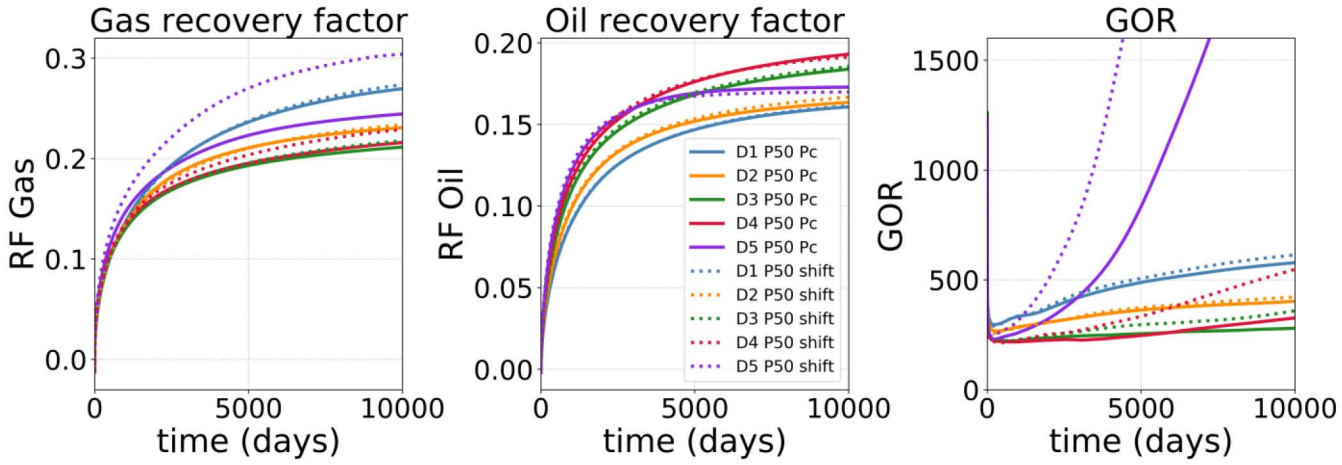

Figure 10—Comparison of production results for different distributions between flash with capillary pressure and flash with critical point shift.

In conclusion, the impact of pore confinement on reservoir production increases the oil production and decreases the gas production and the *GOR* compared with the bulk fluid. It is manifested by two effects: capillary pressure heterogeneity and pore size dependent *PVT* modelling. The impact of capillary pressure

heterogeneity on reservoir production is significant for slightly low percentage of nano-pores (D1 to D3). Large volume of gas might be trapped in very large pores with zero capillary pressure surrounded by tiny pores with high capillary pressure. The impact of pore size dependent *PVT* modeling becomes significant for higher percentage of nano-pores (D4 and D5). The volume of oil with lower bubble point becomes then significant to impact production. The observations are similar for a flash with capillary pressure or a flash with critical point shift. All the results shown in this section comes from reservoir simulations using a very fine grid and can therefore be considered as reliable results. Nonetheless, large scale reservoir simulations need upscaling methodologies because of computational limits. In the following, the fine grid results above will be used as references to compare different coarse grid simulation methodologies.

Upscaling methodology

Dual porosity and MINC models

The understanding and modeling of flow in fractured rocks has been studied since the 1960s (Barenblatt G-I., Zheltov Iu.P. and Kochina I-N. 1960; Warren and Root 1963) and the dual porosity model has been widely used in the petroleum industry since then (Kazemi 1969; Kazemi et al. 1992). This approach replaces the single porosity explicit discrete-fracture approach which is computationally intensive and requires specific details such as fracture and matrix spacial distribution and geometric properties. It therefore may appear natural to use this kind of models for matrix/fracture interaction modeling in unconventional reservoirs (Alharthy et al. 2013). The upscaling of the *PSD* of tight oil and shale gas matrix is very challenging as it is very heterogeneous and many authors chose to use an average pore radius in the matrix (Firincioglu et al. 2013, Sanaei et al. 2014, Haider and Aziz 2017, Alharthy et al. 2017 and Lopez Jimenez et al. 2018). The fine grid simulation results presented in the previous sections are considered as references to compare the dual porosity model with different pore radius. The results for the distribution D2 are shown Figure 11. The modified *EOS* with capillary pressure is used in the matrix subgrid and classic EOS is used in the fracture. The dual porosity model is unable to match the fine grid results for the bulk fluid as well as for the distribution D2.

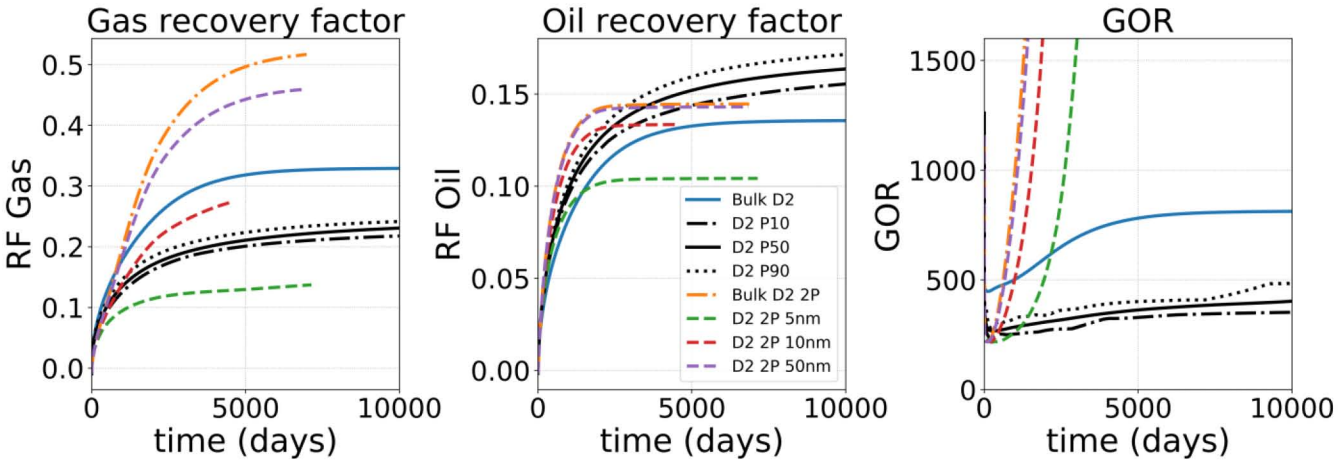

Figure 11—Double porosity model

As the permeability of the matrix is very low, the fracture-matrix interaction shows a long-lasting transient flow (Wu et al. 2012). The quasi-steady state flow assumption of the dual porosity model is then unsuitable to model the matrix-fracture interaction. The more rigorous *MINC* (Multiple Interacting Continua) concept (Narasimhan and Pruess 1988) is adapted as a generalization of the dual-continuum model. It describes pressure gradient between fractures and matrix by further subdividing individual blocks. Figure 12 shows

the results for a dual porosity model with 16 *MINC* subdivisions of the matrix block. The match is very good for the bulk fluid which is showing that the *MINC* method allows modeling the long-lasting transient flow between matrix and fracture. However the dual porosity with *MINC* discretization is still unable to match the fine grid results for the distribution D2 regardless of the pore size value. Considering an average value of the pore size in the matrix with a dual porosity model is therefore unsuitable to model the matrix/fracture interaction with a *PSD* in the matrix. Using saturation dependent effective radius (Liu et al. 2016; Li and Mezzatesta 2017) cannot match the fine grid simulation either, and the obtained results behave like bulk fluid as discussed in the introduction. A triple-porosity model is therefore studied in this paper.

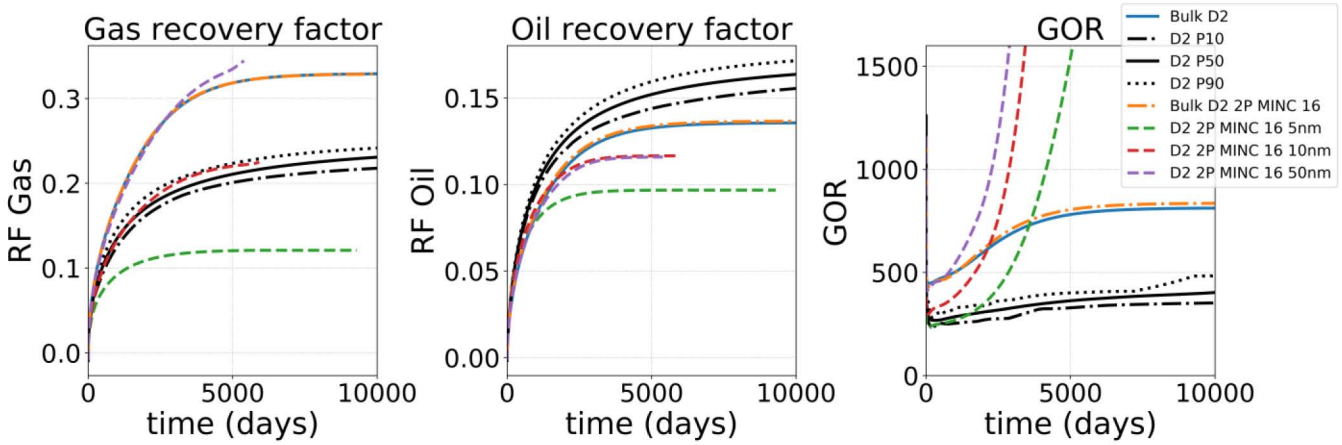

Figure 12—Dual porosity model with *MINC* discretization

Multi-porosity model

The triple porosity or multi porosity model is not new and has been proposed by several authors in the literature for describing flow through fractured rocks. Abdassah and Ershaghi (1986) subdivided the matrix into two subdomains with different porous medium properties. Bai et al. (1993) used a triple porosity model with cracks, fissures and matrix. Liu et al. (2003) considered a model with fractures, rock matrices and cavities. Wu et al. (2004) subdivided the fracture into large fractures and small fractures. More recently these multi-porosity models have been applied to unconventional reservoirs. Wang et al. (2017a) proposed a multi-porosity, multi-physics model for gas flow in shale with five regions: hydraulic fractures, global natural micro-fractures, local micro-fractures, inorganic pores and organic pores. All subdomains have their own properties and fluid flow regime models. For example, gas slippage effect is added in organic and inorganic pores which have also different gas capacities for adsorption, and non-Darcy flow is used for fractures. Wang et al. (2017b) used a triple porosity model for shale gas production simulation. He considered three domains: natural and induced fractures, kerogen-hosted pores of approximately 25nm diameter and kerogen-hosted pores of approximately 1nm diameter. The gas flows from small pores through large pores to fractures. Knudsen diffusion is added in small pores and gas slippage effect is added in large pores. Only Alfi et al. (2017) considered the confined fluid behavior in his triple porosity model. He divided the porous media into three different sub-media: fracture, large pores and small pores. Peng-Robinson *EOS* is used for flash calculation in large pores and fractures, and a modified Peng-Robinson equation of state (Travalloni et al. 2014) is used for small pores with a specific radius. Flow occurs between all the sub-media and thermodynamic equilibrium is verified between small and large pores.

We propose a triple-porosity system modeling matrix/fracture transfers with fractures, small pores and large pores. The flow occurs inside large pores and small pores as illustrated in Figure 13, and only the outmost small pore connects with the fractures. Peng-Robinson *EOS* is used in large pores and fractures, and the modified Peng-Robinson with capillary pressure is used in small pores. The capillary pressure is equal to zero in large pores and it is function of saturation in small pores (Figure 7). The fluid which is predominantly

present in large pores must go through small pores to join the fractures. As the gas-oil capillary pressure of small pore is higher than large pores, the gas flow up to the fracture is slow down. Furthermore as the *PVT* model of the small pore is pore size dependent, then the gas apparition is postponed during depletion. Therefore the two effects of capillary pressure heterogeneity and the confined fluid *PVT* behavior are taken into account in the triple porosity model. The three subdomains have their own porosity and permeability respecting the fine grid properties.

Let ε_{LP} and ε_{SP} be the porosities of large and small pores, they should be constrained by $V_{LP}\varepsilon_{LP}+V_{SP}\varepsilon_{SP} = V_P$, where V_{LP} and V_{SP} correspond to the geometric volume of large and small pores, and V_P is the total porous volume of the matrix block. We assume that the volume fraction of large or small pores (υ_{LP} or υ_{SP}) is a constant everywhere inside the matrix block. For example, for the cases in the previous section, we can consider the volume of large pore corresponds to the part of facies 3 where the pore radius is greater than 100 nm, and the volume of small pore corresponds to the facies 1 and 2. Moreover, let k_{LP} and k_{SP} be the permeabilities of large and small pores, which are used to compute the fluid flow from the inner zone of the matrix block to the fractures. We have $k_{LP} + k_{SP} = k_m$ with k_m the matrix permeability. In case that there are not direct transfers in the large pore medium, in other words, the all large pores are connected through small pores, we have $k_{LP} = 0$ and $k_{SP} = k_m$. One of the challenges in this model is the interaction between large and small pores, which depends on the pore structure, surface exchange areas, etc. We compute this transfer by $F_{LS} = \frac{k_r}{\mu_f} T_{LS}(P_{LP} - P_{SP})$ with T_{LS} the transmissibility, which is proportional to the permeability and exchange surface area and μ_f the fluid viscosity. Let T_{LS0} be the transmissibility between large and small pores in an unit geometric volume, the mass transfer between these two porous media is calculated by $F_{LS} = \frac{k_r}{\mu_f} T_{LS0} V_{cell}(P_{LP} - P_{SP})$, where V_{cell} is the volume of the matrix simulation cell which is composed of both large and small pores. T_{LS0} is a parameter to be determined, and it can be considered as a constant value for a given pore size distribution.

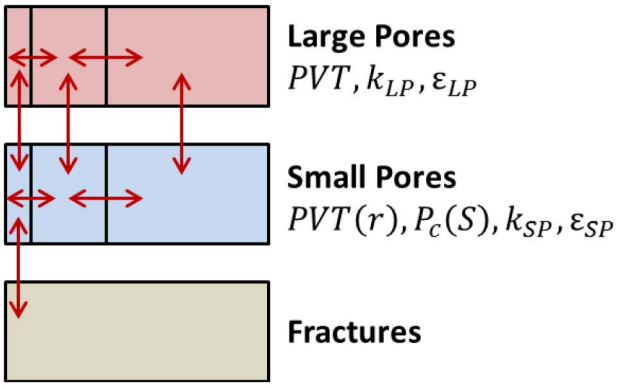

Figure 13—Schematic of *MINC* 1D triple porosity model for one matrix/fracture block

The main parameters to be determined or matched in this triple porosity model are:

- The transmissibility between large and small pores in a unit geometrical volume T_{LS0}.
- The equivalent pore radius in the small pore medium.
- The volume fraction of large or small pores (υ_{LP} or υ_{SP}). In many cases, we can use these fractions calculated directly from their volumes in fine grid scale.
- The matrix permeability in the large pore k_{LP}. In most cases, we can consider $k_{LP} = 0$.

Apart from this triple porosity concept, *MINC* (Multiple Interacting Continua) methodology is also used to discretize the matrix medium. Each *MINC* cell is composed of two parts: a large pore cell and a small pore cell (Figure 13). Only the cell in small pore medium closest to the fracture interacts with the fractures. Coarse grid triple porosity *MINC* simulations (*3P* model) are performed with 16 *MINC* subdivisions to match the fine grid simulations in the previous section for the distributions D1 to D5. The different fitting parameters used for the different distributions D1 to D5 are summarized in Table 6 and the comparison between fine grid and *3P* model are shown in Appendix B (Figure 39 to Figure 43). Figure 14 represents the simulation results with the triple porosity *MINC* approach for D2 which is far better than the dual porosity model.

Table 6—fitting parameters

	r (nm)	k_{LP} *(nD)*	T_{LS0}	*small pores grid volume fraction (%)* v_{SP}
D1	20	30	$2*10^{-20}$	**0.65**
D2	8	3	$8*10^{-21}$	0.41
D3	3.5	0	$3.08*10^{-20}$	0.6
D4	5	0	$8*10^{-20}$	0.7
D5	10	0	$8*10^{-20}$	**0.75**

Concerning the fitting parameters (Table 6), when the proportion of nanopores is low like in D1, large volume of gas can be connected together without being separated by small pores. This is not the case when the proportion of nanopores becomes high like in D3, D4, and D5. That is why the large pore permeability k_{LP} is not equal to zero for D1 and D2. In order to keep the pore volume constant, equation 15 is used to calculate large pore porosity in case of small pores grid volume fraction change v_{SP}. If v_{SP} is not changed then $\varepsilon_{LP} = \varepsilon_{f3}$. The fitting parameter v_{SP} is only used for D1 and D5. v_{SP} for D1 is changed from 0.3 to 0.65 and v_{SP} for D5 is changed from 0.85 to 0.75. When the proportion of small pores is too low like D1, an adjustment might be necessary by increasing its volume in the coarse grid model. On the other hand, if the proportion of small pores is too high, it might be more convenient for an adjustment by reducing its volume in the triple porosity model.

$$\begin{cases} \varepsilon_{SP} = \dfrac{v_{f1}\varepsilon_{f1} + v_{f2}\varepsilon_{f2}}{v_{f1} + v_{f2}} \\ \varepsilon_{LP+SP} = \varepsilon_{f1}v_{f1} + \varepsilon_{f2}v_{f2} + \varepsilon_{f3}v_{f3} \\ \varepsilon_{LP} = \dfrac{\varepsilon_{LP+SP} - v_{SP}\varepsilon_{SP}}{1 - v_{SP}} \end{cases} \quad (15)$$

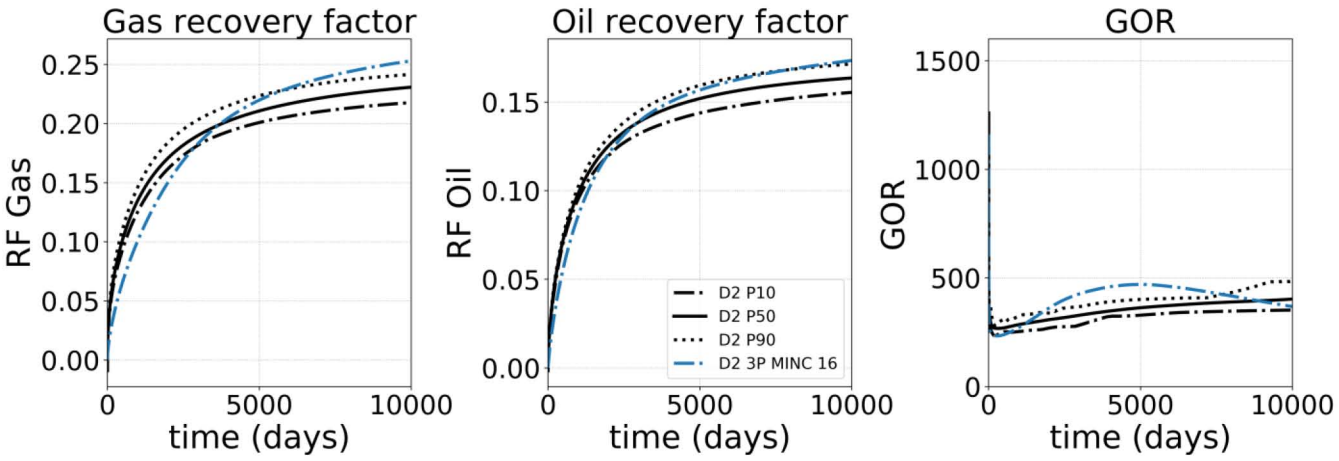

Figure 14—triple porosity model with matching of D2

An upscaled model of the matrix/fracture interaction has been fitted for each of the five distributions D. A large scale reservoir simulation case can therefore be built with this triple porosity model by discretizing the fracture medium with a standard method used in the dual-porosity approach.

Simulation of a fractured well in a stimulated reversoir volume (SRV)

The reservoir simulation at *SRV* scale is generally made with a single and a dual porosity model with a discrete pore size distribution of one value per cell or an average pore radius (Firincioglu et al. 2013; Sanaei et al. 2014; Alharthy et al. 2017; Haider and Aziz 2017; Lopez Jimenez et al. 2018). We propose here to apply the triple porosity model presented above to a large scale reservoir simulation of a horizontal producing well in a *SRV*.

Reservoir model

A *SRV* simulation case has been built according to Figure 15 with one horizontal well in the center. The 2D grid is 2000m length and 1300m width and the cell dimensions in the x, y and z directions are 100m*100m*10m. The fracture spacing is 20 m in x and y directions, and the corresponding block size of 20×20 m is used for the matrix-fracture transfer modeling. The fracture permeability in the well blocks is fixed to 100D and the remaining *SRV* have an equivalent fracture permeability of 0.01D and 0.001D as illustrated in Figure 15. The upscaled parameters are the same as the one presented in Table 6. Furthermore the *MINC* discretization in the small and large pores is now made in two dimensions with 16 cells in the matrix medium (16 cells in the marge pore medium and 16 cells in the small pore medium) as represented in Figure 16.

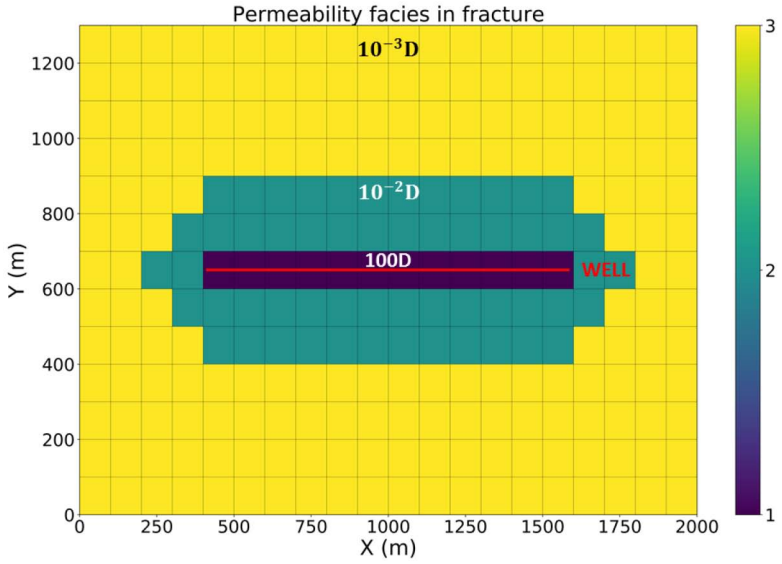

Figure 15—*SRV* fracture grid

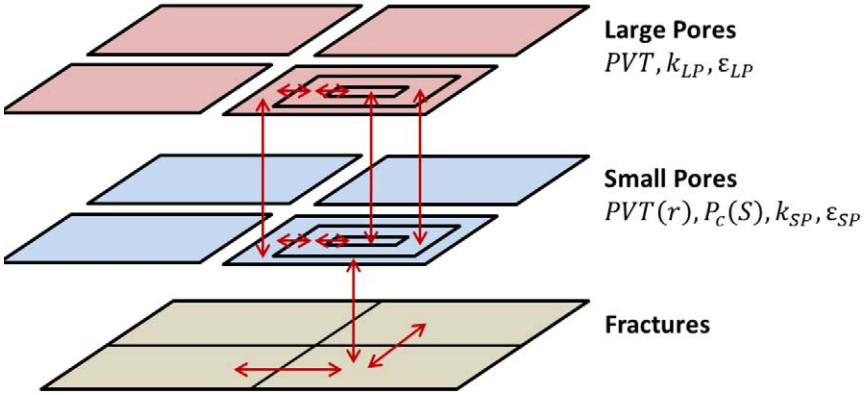

Figure 16—Schematic of *MINC* triple porosity model for *SRV* simulation

SRV simulation for the distribution D2

It is assumed that the pore size distribution in the matrix medium corresponds to that of D2. The fitted parameters given in Table 6 are used for the triple porosity *MINC* simulation. The production simulation results are presented Figure 17 together with those obtained by the dual-porosity *MINC* method. The bulk curves correspond to the simulation result of a dual porosity *MINC* method with zero capillary pressure and classic Peng Robinson EOS. The "*D2 2P MINC*" model corresponds to a dual porosity model and *MINC* method with capillary pressure given Figure 7 for the flow in the matrix and a flash with capillary pressure with the same radius as used in the small pores of the fitted triple porosity model. The differences between the triple-porosity *MINC* simulation and the dual-porosity *MINC* simulation, which is usually used in the literature to study nanopore *PVT* behavior in tight oil and shale gas reservoirs, are very large. We believe that the triple porosity approach gives more reliable results, and the dual porosity model is not very accurate to handle the pore size distribution issue. As observed at matrix/fracture interaction scale, the pore confinement representing by the "*D2 3P MINC*" model increased oil production and decreases gas production and *GOR*. This trend is not represented by the "*D2 2P MINC*" model mostly used in the literature.

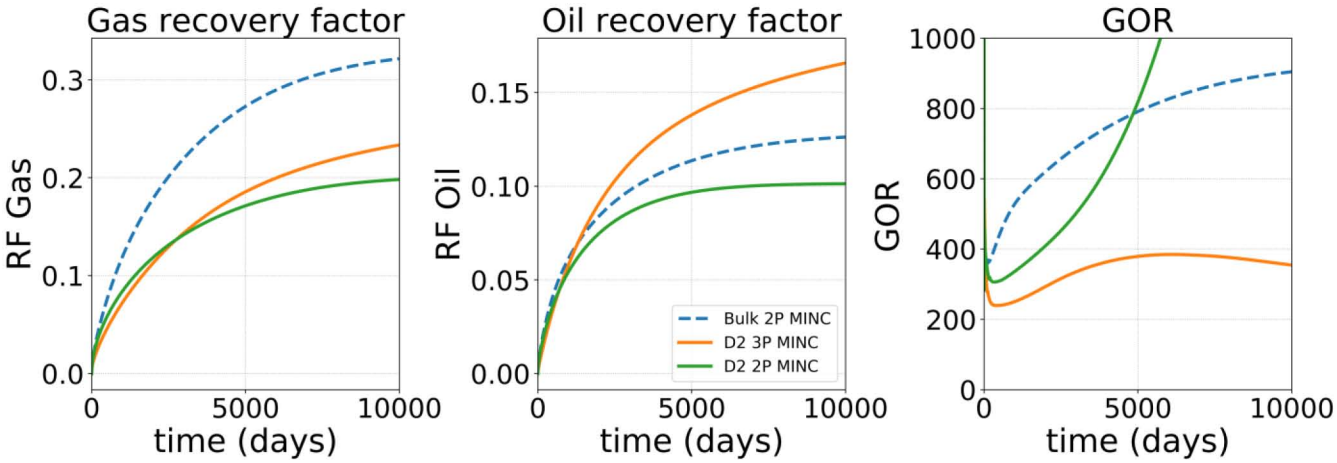

Figure 17—Production results of the *SRV* with distribution D2

SRV simulation for a distribution of D

A second *SRV* model has been built for a random realisation of the different distributions D1, D2, D3, D4, D5 represented in Figure 18. The distribution corresponds to a grid fraction of 15% of D1, 40% of D2, 10% of D3, 15% of D4 and 20% of D5. The different fitted parameters of the triple porosity model for the different distribution D (Table 6) has been used in this simulation. Figure 19 represents the production results for bulk in a dual porosity *MINC* method ("*Bulk 2P MINC*") and for confined fluid in both dual porosity *MINC* method ("*D distribution 2P MINC*") and the triple porosity model ("*D distribution 3P MINC*"). As discussed previously, the "*Bulk 2P MINC*" model corresponds to a dual porosity model and *MINC* method with zero capillary pressure in the matrix and different porosities (or *PSD*) in each cell. The "*D distribution 2P MINC*" model corresponds to a dual porosity model and *MINC* method with capillary pressure in the matrix (Figure 7), different porosities and pore radius in each cells in accordance to the corresponding *PSD*. The confined "*D distribution 3P MINC*" model corresponds to the triple porosity *MINC* model with *MINC* discretization using upscaled parameters according to the cell *PSD*. The results are quite similar to the previous case with a single distribution D2. We have the same conclusion with an increasing of oil production and a decreasing of gas production and *GOR*.

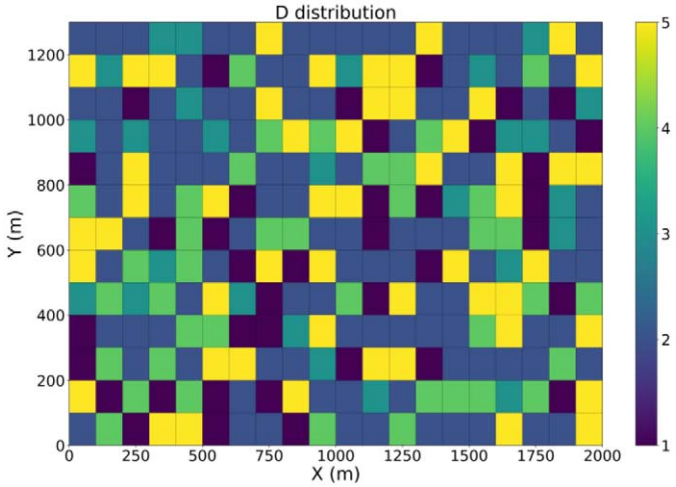

Figure 18—Spacial distribution of D1, D2, D3, D4, and D5

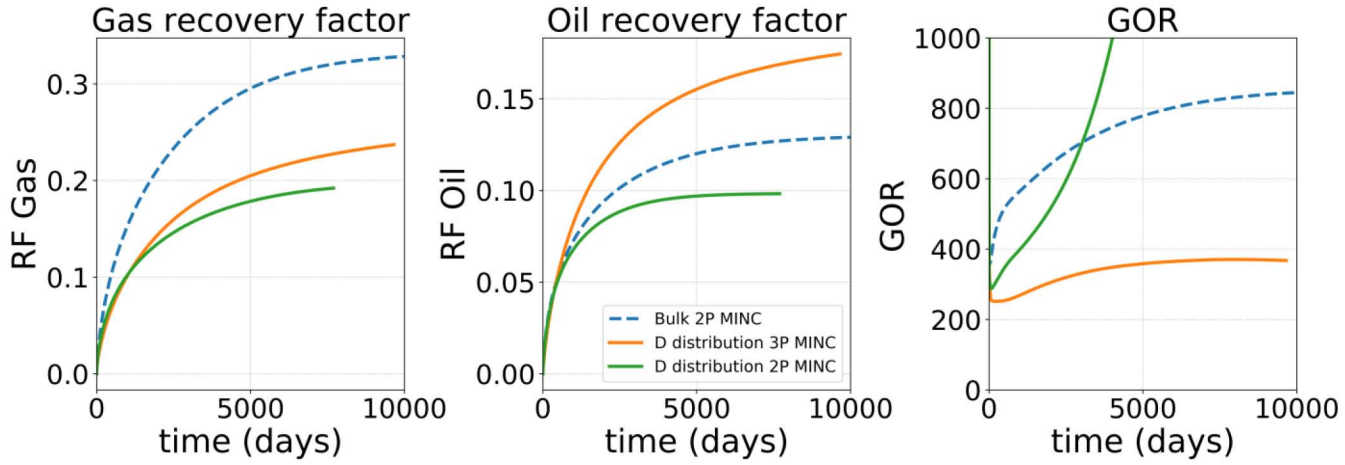

Figure 19—Production results of the *SRV* with spacial distribution of D1, D2, D3, D4, and D5

Pressures and saturation fields have been plotted in Figure 20 for a specific time (980 days) in each sub domains of the triple porosity model: fracture, small pore and large pore. The gas saturation is higher in large pore than in small pore because the bubble point is decreased in small pore due to the pore dependent *PVT* behavior. The gas pressure is higher than the oil pressure only in small pore because of capillary pressure which is zero in large pore and is a function of saturation in small pore. This participates to slow down the gas flow from large pore to fracture through small pore compare to bulk where capillary pressure is zero in the entire matrix. This example shows the effect of pore size dependent *PVT* behavior and capillary pressure heterogeneity taken into account in the triple porosity model.

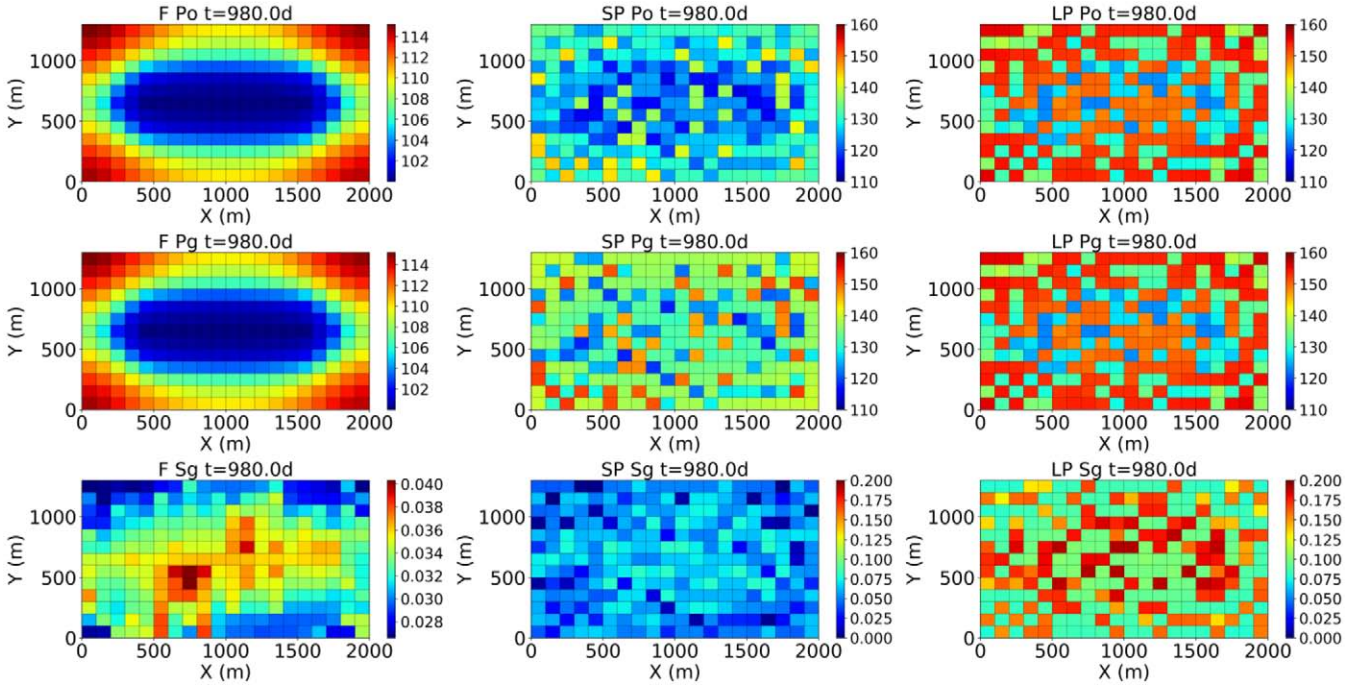

Figure 20—Oil, gas pressure field and saturation field in fracture (F), large pore (LP) and small pore (SP) of the triple porosity model at 980 days.

Discussions

We have presented a general methodology to upscale the nanopore size dependent *EOS* and pore size distribution for a coarse grid triple porosity *MINC* model. But in the examples of this paper, we are limited to small upscaling domains.

In this work, the triple porosity model parameters are matched from a 2D rectilinear flow simulation. We assume that the fitted parameters, such as the transmissibility between large and small pores in an unit volume, the equivalent pore radius in the small pore medium, the volume fracture of large and small pore, and the permeability in the large pore, are intrinsic properties related only to the pore size distributions, and they do not depend on the matrix block sizes as well as multi-directional exchange between matrix and fractures.

A drawback of the present work is that the considered upscaling domain is not very large. The generated spatial pore size distribution might be not representative, and the complexity of pore connections is not correctly modeled. In this work, the considered domain is relatively small, and the flow is rectilinear. Nano and mesopores can easily form a spatial barrier to enhance the nanopore effect. In a large domain, the effect related to barrier might be different, and this has an impact on spatial pore size distribution and flow fluid behavior. In the next step, we will study large upscaling domains, such as two dimensional matrix block or three dimensional fine grid pore size distributions, where the pore connections are better modeled.

Conclusions

The effect of pore confinement on hydrocarbon thermodynamic properties, the impact of *PSD* on reservoir production and finally *PSD* upscaling methodologies for large scale reservoir simulations have been studied in this paper.

PVT behavior of pure components and mixtures confined in slit graphite pores have been studied using a new workflow involving at the end a modified version of the *GEMC NVT* simulation adding interactions between the surface walls and the fluid molecules. The critical temperature and pressure of pure components are reduced, compared to the bulk fluid, as the pore width decreases. Their evolution of the critical temperature and pressure versus pore length follows different trends and they can be modeled by different correlations proposed in the literature (Jin et al. (2013) for critical temperature and Meyra et al. (2005) for critical pressure). Concerning the density of pure components and mixtures, regardless of the composition, the vapor density is increased and the liquid density is decreased with confinement compared to bulk. The bubble point is decreased and the dew point is increased with confinement. These reference data have been compared to the most commonly used *PVT* modified *EOS* model in the literature which are flash with capillary pressure and flash with critical point shift. The best match between molecular simulations and *EOS* results are obtained with the flash with both capillary pressure and critical point shift.

The *PSD* impact on production has been studied on matrix/fracture interactions with a fine grid single-porosity simulation by considering the effect of nanopores. The *PSD* is based on three facies with their own pore radius range, porosity and capillary pressure. Five *PSD* are considered with different pore volume per facies describing from low nanopores proportion to high nanopores proportion in the matrix. For each of the five *PSD*, ten different realisations are given. Regardless of the *PSD*, confinement increases the oil production and decreases the gas production and *GOR*. In a *PSD*, the confinement is characterized by two effects, capillary pressure heterogeneity and *PVT* in nanopores. In low fraction of nanopores inside the matrix, and the flash effect is negligible. Because of the higher capillary pressure nanopores compared to large pores, an important volume of gas stay stuck in the large pores. The pore radius dependent *EOS* becomes important for high fraction of nanopores inside the matrix. The bubble point of fluid inside nanopores is decreased, and then a large quantity of gas apparition is postponed during depletion. Comparing the different *PSD*, the oil production is increased and the gas production and *GOR* is decreased when the fraction of nanopores inside the matrix increases. But for very high fraction of nanopores, the trend is

different and reverses itself, marking the transition of the importance of the two effects. The conclusions here are similar for a reservoir model using a flash with capillary pressure or a shift of critical pressure and temperature.

Several coarse grid simulation models have been studied on synthetic cases with different *PSD*. Comparing the coarse grid results with reference fine grid simulations allows to concluding about the relevance of the upscaling model. The commonly-used dual porosity *MINC* model with an average pore radius of the literature (whatever the pore radius size) is unable to match the fine grid results. A triple porosity model has been built with three domains: fracture, small pores and large pores. The flow goes from the large pores to the fracture through the small pores. Large pore domain has a classic Peng Robinson *EOS* and the small pore domain has a modified Peng Robinson *EOS* with capillary pressure and a capillary pressure function of saturation for the flow. The two effects of capillary pressure heterogeneity and pore radius dependent EOS are therefore taken into account in the upscaled model. A *MINC* discretization is performed in the matrix medium with a fixed fraction of small pores and large pores for a given *PSD*, and the flow transfer is considered both inside them and between them. A fitting of every *PSD* fine grid results has been done with the triple porosity model using fitting parameters as large pores/small pores transmissibility in a unit volume, pore radius, sub domains permeability and small pore volume fraction.

A large scale *SRV* model has been built by taking into account the pore size distribution and its spatial variation on the simulation cells, and has been simulated with different coarse grid models. The triple porosity approach has shown quite different results, compared to the commonly-used dual porosity models with an equivalent nanopore radius. We believe that the triple porosity approach is more suitable for the handling of complex physics in nanoporous reservoirs, and gives more reliable results. An increase of oil production and a decrease in gas production and *GOR* is observed compare to the bulk, which is not the case for a dual porosity model.

Nomenclature

A = *Peng Robinson cubic EOS coefficient*
B = *Peng Robinson cubic EOS coefficient*
dx = *cell length in the X-direction, m*
dy = *cell length in the Y-direction, m*
dz = *cell length in the Z-direction, m*
f_{l_i} = *liquid fugacity of component i*
f_{v_i} = *vapor fugacity of component i*
F_{LS} = *Flux between large pore and small pore, m³/s*
H = *slit pore width, nm*
K_i = *equilibrium constant of component i*
k = *permeability (D)*
k_{SP} = *permeability of small pore, D*
k_{LP} = *permeability of large pore, D*
k_m = *matrix permeability, D*
k_r = *relative permeability*
L = *molar fraction of liquid phase*
M_i = *molar mass of component i, g/mol*
N_{av} = *Avogadro number*
$<N_i>$ = *average number of component i*
P_c = *critical pressure, Pa*
P_{cap} = *capillarity pressure, Pa*

P_i = Parachor of component i, (dyne$^{1/4}$-cm$^{11/4}$)/mol
P_l = Parachor of liquid phase, (dyne$^{1/4}$-cm$^{11/4}$)/mol
P_v = Parachor of vapor phase, (dyne$^{1/4}$-cm$^{11/4}$)/mol
P^l = liquid pressure, Pa
P^v = Vapor pressure, Pa
P_{LP} = Large pore pressure, Pa
P_{SP} = Small pore pressure, Pa
r_{sf} = distance between solid and fluid particles, Å
r = pore radius (nm)
T = temperature, K
T_c = critical temperature, K
T_{LS} = Transmissibility between large pore and small pore, m³
T_{LS0} = Transmissibility between large pore and small pore in a unit geometric volume
u_{sf} = Steele 9-3 potential between solid and fluid, J
V_{LP} = geometric volume of large pore, m³
V_{SP} = geometric volume of small pore, m³
V_{cell} = volume of cell, m³
V = molar fraction of vapor phase
V_{box} = volume of the simulation box, nm³
υ_{LP} =volume fraction of large pore
υ_{SP} =volume fraction of small pore
υ_{fi} =volume fraction of facies i
x_i = liquid molar fraction of component i
y_i = vapor molar fraction of component i
z_i = molar fraction of component i
Z = compressibility factor

Greek Symbols

ε = depth of potential well, J
ε_{fi} = porosity of facies i
ε_{LP} = large pore porosity
ε_{SP} = small pore porosity
θ = contact angle
μ = chemical potential, J
μ_f = viscosity, kg/(m.s)
ρ_s = atomic density of solid, kg/m3
ρ_i = density of component i, kg/m3
ρ_l = liquid density, kg/m3
ρ_v = vapor density, kg/m3
ρ_c = critical density, kg/mol
σ_{VL} = interfacial tension between liquid and vapor, dyn/cm
σ = distance between particles where inter particles potential is zero, Å
Φ_i = fugacity coefficient of component i
ω_i = acentric factor of component i

Subscript

l = *liquid*
v = *vapor*
x = *X-direction*
y = *Y-direction*
z = *Z-direction*

Acronyms

BPMC = *Bubble Point Monte Carlo pseudo ensemble*
CP = *Critical point*
EOS = *Equation Of State*
GOR = *Gas Oil Ratio*
GCMC = *Grand Canonical Monte Carlo*
GEMC = *Gibbs Ensemble Monte Carlo*
IFT = *Interfacial tension*
LJ = *Lennard-Jones*
LP = *Large Pore*
MINC = *Multiple Interacting Continua*
NPT = *GCMC ensemble with number of particles, pressure and temperature constant*
NVT = *GEMC ensemble with total number of particles, total volume and temperature T constant*
μVT = *GCMC ensemble with fugacity, volume and temperature constant*
PVT = *Pressure-Volume-Temperature*
PSD = *Pore Size Distribution*
SP = *Small Pore*
SRV = *Stimulated Reservoir Volume*
2P = *dual porosity model*
3P = *triple porosity model*

References

Abdassah, D. and Ershaghi, I.1986. Triple-Porosity Systems for Representing Naturally Fractured Reservoirs. *SPE Formation Evaluation* **1** (02): 113–127. https://doi.org/10.2118/13409-PA.

Alfi, M., An, C., Cao, Y. et al 2017. *Pore Size Variability and Sieving Effect in Liquid Shale—A Multiple Permeability Approach and Eagle Ford Case Study*. https://doi.org/10.2118/182643-MS.

Alfi, M., Nasrabadi, H., and Banerjee, D.2016. Experimental investigation of confinement effect on phase behavior of hexane, heptane and octane using lab-on-a-chip technology. *FLUID PHASE EQUILIBR* **423**: 25–33. https://doi.org/10.1016/j.fluid.2016.04.017.

Alharthy, N. S., Nguyen, T., Teklu, T. et al 2013. *Multiphase Compositional Modeling in Small-Scale Pores of Unconventional Shale Reservoirs*. Richardson, TX. https://doi.org/10.2118/166306-MS.

Alharthy, N. S., Teklu, T. W., Abd El-Gawad, S. et al 2017. *Flow Dynamics and Pore Scale Physics in Unconventional Shale Reservoirs*.

Bai, M., Elsworth, D., and Roegiers, J.C. 1993. Multiporosity/multipermeability approach to the simulation of naturally fractured reservoirs. *Water Resources Research* **29** (6): 1621–1633. https://doi.org/10.1029/92WR02746.

Barbosa, G. D., Travalloni, L., Castier, M. et al 2016. Extending an equation of state to confined fluids with basis on molecular simulations. *Chemical Engineering Science* **153**: 212–220. https://doi.org/10.1016/j.ces.2016.07.033.

Barenblatt G-I., Zheltov Iu.P. and Kochina I-N. (ed.). 1960. *Basic concept in the theory of seepage of homogeneous liquids in fissured rocks*. Society of Exploration Geophysicists, American Association of Petroleum Geologists, Society of Petroleum Engineers. https://doi.org/10.1190/URTEC2013.

Bourasseau, E., Ungerer, P., Boutin, A. et al 2002. Monte Carlo simulation of branched alkanes and long chain n -alkanes with anisotropic united atoms intermolecular potential. *molecular simulation*.

BP. 2017. *BP Energy outlook*.

Cho, H., Bartl, M. H., and Deo, M. 2017. Bubble Point Measurements of Hydrocarbon Mixtures in Mesoporous Media. *Energy Fuels*. https://doi.org/10.1021/acs.energyfuels.6b02424.

Curtis H. Whitson and Michael L. Michelsen. 1989. The negative flash. *Fluid Phase Equilibria* **53**: 51–71. https://doi.org/10.1016/0378-3812(89)80072-X.

Daan Frenkel and Berend Smit. 1996. *Understanding Molecular Simulation: From Algorithms to Applications*. Elsevier.

Devegowda, D., Sapmanee, K., Civan, F. et al 2012. *Phase Behavior of Gas Condensates in Shales Due to Pore Proximity Effects: Implications for Transport, Reserves and Well Productivity*. Richardson, Tex. https://doi.org/10.2118/160099-MS.

Dong, X., Liu, H., Hou, J. et al 2012. Phase Behavior of Hydrocarbon Mixtures in the Organic Nanopores of Unconventional Gas Condensate Reservoirs. In *Granites and basalts: Questionable paradigms*, firstst ed., ed. V. Sánchez Cela. Zaragoza: University of Zaragoza. https://doi.org/10.15530/URTEC-2016-2460485.

Dong, X., Liu, H., Hou, J. et al 2016. Phase Equilibria of Confined Fluids in Nanopores of Tight and Shale Rocks Considering the Effect of Capillary Pressure and Adsorption Film. *Ind. Eng. Chem. Res.* **55** (3): 798–811. https://doi.org/10.1021/acs.iecr.5b04276.

ExxonMobil. 2018. *2018 Outlook for Energy: A View to 2040*.

Ferrando, N., Defiolle, D., Lachet V. et al 2010. Ethanoled gasoline bubble pressure determination: Experimental and Monte Carlo modeling. *Fluid Phase Equilibria* **299** (1): 132–140. https://doi.org/10.1016/j.fluid.2010.09.020.

Firincioglu, T., Ozgen, C., and Ozkan, E.2013. *An Excess-Bubble-Point-Suppression Correlation for Black Oil Simulation of Nano-Porous Unconventional Oil Reservoirs*. Richardson, TX. https://doi.org/10.2118/166459-MS.

Firincioglu, T., Ozkan, E., and Ozgen, C.2012. Thermodynamics of Multiphase Flow in Unconventional Liquids-Rich Reservoirs. Richardson, Tex. https://doi.org/10.2118/159869-MS.

Gelb, L. D., Gubbins, K. E., Radhakrishnan, R. et al 1999. Phase separation in confined systems. *Rep. Prog. Phys.* **62** (12): 1573. https://doi.org/10.1088/0034-4885/62/12/201.

Haider, B. A. and Aziz, K.2017. *Impact of Capillary Pressure and Critical Property Shift due to Confinement on Hydrocarbon Production in Shale Reservoirs*. https://doi.org/10.2118/182603-MS.

Islam, A. W. and Sun, A. Y.2016. A theory-based simple extension of Peng–Robinson equation of state for nanopore confined fluids. *J Petrol Explor Prod Technol:* 1–7. https://doi.org/10.1007/s13202-016-0306-y.

Jiang, S. and Gubbins, K.1995. Vapor-liquid equilibria in two-dimensional Lennard-Jones fluids: Unperturbed and substrate-mediated films. *Molecular Physics - MOL PHYS* **86**: 599–612. https://doi.org/10.1080/00268979500102221.

Jin, B., Bi, R., and Nasrabadi, H.2017. Molecular simulation of the pore size distribution effect on phase behavior of methane confined in nanopores. *Fluid Phase Equilibria* **452**: 94–102. https://doi.org/10.1016/j.fluid.2017.08.017.

Jin, B. and Nasrabadi, H.2018. Phase Behavior in Shale Organic/Inorganic Nanopores From Molecular Simulation. *SPE Reservoir Evaluation & Engineering* **21** (03): 626–637. https://doi.org/10.2118/187307-PA.

Jin, L., Ma, Y., and Jamili, A.2013. *Investigating The Effect of Pore Proximity on Phase Behavior And Fluid Properties in Shale Formations*. Richardson, TX. https://doi.org/10.2118/166192-MS.

Kazemi, H. 1969. Pressure Transient Analysis of Naturally Fractured Reservoirs with Uniform Fracture Distribution. *Society of Petroleum Engineers Journal* **9** (04): 451–462. https://doi.org/10.2118/2156-A.

Kazemi, H., Gilman, J. R., and Elsharkawy, A. M.1992. Analytical and Numerical Solution of Oil Recovery From Fractured Reservoirs With Empirical Transfer Functions (includes associated papers 25528 and 25818). *SPE Reservoir Engineering* **7** (02): 219–227. https://doi.org/10.2118/19849-PA.

Kuila, U. and Prasad, M.2011. Understanding Pore-Structure And Permeability In Shales. In *ATCE 2011*. https://doi.org/10.2118/146869-MS.

Kuila, U. and Prasad, M.2013. Specific surface area and pore?size distribution in clays and shales. *Geophysical Prospecting* **61** (2): 341–362. https://doi.org/10.1111/1365-2478.12028.

Kumar, S., Hoffman, T., and Prasad, M. (eds.). 2013. *Upper and Lower Bakken Shale Production Contribution to the Middle Bakken Reservoir*. https://doi.org/10.1190/urtec2013-001.

Lambert J. Van Poolen, Cynthia D. Holcomb, Vicki G. Niesen. 1997. Critical temperature and density from liquid-vapor coexistence data: Application to refrigerants R32, R124, and R152a. *Fluid Phase Equilibria* **129** (1-2): 105–111. https://doi.org/10.1016/S0378-3812(96)03171-8.

Li, B. and Mezzatesta, A.2017. *Evaluation of Pore Size Distribution Effects on Phase Behavior of Hydrocarbons Produced in Shale Gas Condensate Reservoirs*. https://doi.org/10.2118/183833-MS.

Li, B., Mezzatesta, A., Li, Y. et al 2016. *A Multilevel Iterative Method to Quantify Effects of Pore-Size Distribution on Phase Equilibrium of Multicomponent Fluids in Unconventional Plays*. *Petrophysics* **57** (02).

Liu, J., Bodvarsson, G. S., and Wu, Y.-S.2003. Analysis of flow behavior in fractured lithophysal reservoirs. *Journal of Contaminant Hydrology* **62-63**: 189–211. https://doi.org/10.1016/S0169-7722(02)00169-9.

Liu, Y., Li, H. A., and Okuno, R.2016. *Phase Behavior of Fluid Mixtures in a Partially Confined Space*. https://doi.org/10.2118/181716-MS.

Lopez Jimenez, B. A., Hernandez, G., Czernia, B. et al 2018. *Effects of Thermodynamic and Rock Properties on the Performance of Liquids-Rich Nano-Porous Shale Reservoirs*. Society of Petroleum Engineers. https://doi.org/10.2118/191813-MS.

Luo, S., Nasrabadi, H., and Lutkenhaus, J. L.2016. Effect of confinement on the bubble points of hydrocarbons in nanoporous media. *AIChE Journal* **62** (5): 1772–1780. https://doi.org/10.1002/aic.15154.

Meyra, A. G., Zarragoicoechea, G. J., and Kuz, V. A.2005. Thermodynamic equations for a confined fluid at nanometric scale. *Fluid Phase Equilibria* **230** (1–2): 9–14. https://doi.org/10.1016/j.fluid.2004.10.014.

Narasimhan, T. N. and Pruess, K.1988. MINC: An Approach for Analyzing Transport in Strongly Heterogeneous Systems. In *Groundwater flow and quality modelling*, ed. E. Custodio, A. Gurgui, and J. P. L. Ferreira. 375–391. [Place of publication not identified]: Springer. https://doi.org/10.1007/978-94-009-2889-3_21.

Nelson, P. H. 2009. Pore-throat sizes in sandstones, tight sandstones, and shales. *AAPG Bulletin* **93** (3): 329–340. https://doi.org/10.1306/10240808059.

Nojabaei, B., Johns, R. T., and Chu, L.2013. Effect of Capillary Pressure on Phase Behavior in Tight Rocks and Shales. *SPE Reservoir Evaluation & Engineering* **16** (03): 281–289. https://doi.org/10.2118/159258-PA.

Nojabaei, B., Siripatrachai, N., Johns, R. T. et al 2014. *Effect of Saturation Dependent Capillary Pressure on Production in Tight Rocks and Shales: A Compositionally-Extended Black Oil Formulation*. Richardson, Texas: Society of Petroleum Engineers. https://doi.org/10.2118/171028-MS.

Panagiotopoulos, A. Z. 1986. Direct determination of phase coexistence properties of fluids by Monte Carlo simulation in a new ensemble. *Molecular Physics*.

Panagiotopoulos, A. Z. 1987. Adsorption and capillary condensation of fluids in cylindrical pores by Monte Carlo simulation in the Gibbs ensemble. *Molecular Physics*.

Panagiotopoulos, A. Z., Quirke, N., Stapleton, M. et al 1987. Phase equilibria by simulation in the Gibbs ensemble. *Molecular Physics*.

Péneloux, A., Rauzy, E., and Fréze, R. 1982. A consistent correction for Redlich-Kwong-Soave volumes. *Fluid Phase Equilibria* **8** (1): 7–23. https://doi.org/10.1016/0378-3812(82)80002-2.

Peng, D.-Y. and Robinson, D. B.1976. A New Two-Constant Equation of State. *Ind. Eng. Chem. Fund.* **15** (1): 59–64. https://doi.org/10.1021/i160057a011.

Pitakbunkate, T., Balbuena, P. B., Moridis, G. J. et al 2016. Effect of Confinement on Pressure/Volume/Temperature Properties of Hydrocarbons in Shale Reservoirs. *SPE Journal* **21** (02): 621–634. https://doi.org/10.2118/170685-PA.

Pitakbunkate, T., Blasingame, T. A., Moridis, G. J. et al 2017. Phase Behavior of Methane–Ethane Mixtures in Nanopores. *Ind. Eng. Chem. Res.* **56** (40): 11634–11643. https://doi.org/10.1021/acs.iecr.7b01913.

Pommer, M. E. 2014. *Quantitative assessment of pore types and pore size distribution across thermal maturity*, Eagle Ford Formation, South Texas (2014).

Porcheron, F., Rousseau, B., Fuchs, A. H. et al 1999. Monte Carlo simulations of nanoconfined n-decane films. *Phys. Chem. Chem. Phys.* **1** (17): 4083–4090. https://doi.org/10.1039/A903431E.

Rahmani Didar, B. and Akkutlu, I. Y.2015. *Confinement Effects on Hydrocarbon Mixture Phase Behavior in Organic Nanopore*. Society of Petroleum Engineers. https://doi.org/10.2118/178519-MS.

Rezaveisi, M., Sepehrnoori, K., Pope, G. A. et al 2015. Compositional Simulation Including Effect of Capillary Pressure on Phase Behavior. In *Annual Technical Conference and Exhibition: "vibrant vision, new perspective"s, conference proceedings*, Houston, Texas, 28-30 September 2015, George R. Brown Convention Center. Richardson, Tex.: Society of Petroleum Engineers. https://doi.org/10.2118/175135-MS.

Sanaei, A., Jamili, A., and Callard, J.2014. Effect of Pore Size Distribution and Connectivity on Phase Behavior and Gas Condensate Production From Unconventional Resources. [Richardson, Tex.]: Society of Petroleum Engineers. https://doi.org/10.2118/168970-MS.

Sandoval, D. R., Yan, W., Michelsen, M. L. et al 2016. The Phase Envelope of Multicomponent Mixtures in the Presence of a Capillary Pressure Difference. *Ind. Eng. Chem. Res.* **55** (22): 6530–6538. https://doi.org/10.1021/acs.iecr.6b00972.

Shaoyi, J. and Keith E., G. 1995. *Vapour-liquid equilibria in two-dimensional Lennard-Jones fluids: unperturbed and substrate-mediated filMS*.

Shapiro, A. and Stenby, E. H.2001. Thermodynamics of the multicomponent vapor-liquid equilibrium under capillary pressure difference. *FLUID PHASE EQUILIBR* **178** (1-2): 17–32.

Siderius, D. W. and Gelb, L. D.2011. Extension of the Steele 10-4-3 potential for adsorption calculations in cylindrical, spherical, and other pore geometries. *J Chem Phys* **135** (8): 84703. https://doi.org/10.1063/1.3626804.

Singh, S. K. and Singh, J. K.2011. Effect of pore morphology on vapor–liquid phase transition and crossover behavior of critical properties from 3D to 2D. *Fluid Phase Equilibria* **300** (1–2): 182–187. https://doi.org/10.1016/j.fluid.2010.10.014.

Singh, S. K., Sinha, A., Deo, G. et al 2009. Vapor-Liquid Phase Coexistence, Critical Properties, and Surface Tension of Confined Alkanes. *J. Phys. Chem. C* **113** (17): 7170–7180. https://doi.org/10.1021/jp8073915.

Sobecki, N., Nieto Draghi, C., Di Lella, A. et al 2019. *Phase behavior of hydrocarbons in nano-pores, submitted*.

Steele, W. A. 1973. The physical interaction of gases with crystalline solids: I. Gas-solid energies and properties of isolated adsorbed atoms. *Surface Science* **36** (1): 317–352. https://doi.org/10.1016/0039-6028(73)90264-1.

Stimpson, B. C. and Barrufet, M. A.2016. Effects of Confined Space on Production from Tight Reservoirs. https://doi.org/10.2118/181686-MS.

Teklu, T. W., Alharthy, N., Kazemi, H. et al 2014. Phase Behavior and Minimum Miscibility Pressure in Nanopores. *SPE Reservoir Evaluation & Engineering* **17** (03): 396–403. https://doi.org/10.2118/168865-PA.

Tian, Y., Ayers, W. B., and McCain, W. D.2013. The Eagle Ford Shale Play, South Texas: Regional Variations in Fluid Types, Hydrocarbon Production and Reservoir Properties. In International Petroleum Technology Conference. International Petroleum Technology Conference. https://doi.org/10.2523/IPTC-16808-MS.

Travalloni, L., Castier, M., Tavares, F. W. et al 2010. Critical behavior of pure confined fluids from an extension of the van der Waals equation of state. *The Journal of Supercritical Fluids* **55** (2): 455–461. https://doi.org/10.1016/j.supflu.2010.09.008.

Travalloni, L., Castier, M., and Tavares, F. W.2014. Phase equilibrium of fluids confined in porous media from an extended Peng–Robinson equation of state. *Fluid Phase Equilibria* **362**: 335–341. https://doi.org/10.1016/j.fluid.2013.10.049.

U.S. Energy Information Administration. 2016. *International Energy Outlook 2016*.

U.S. Energy Information Administration. 2017. *International Energy Outlook 2017*.

Ungerer, P., Beauvais, C., Delhommelle, J. et al 2000. Optimization of the anisotropic united atoms intermolecular potential for n -alkanes. *J Chem Phys* **112** (12): 5499–5510. https://doi.org/10.1063/1.481116.

Ungerer, P., Boutin, A., and Fuchs, A. H.1999. Direct calculation of bubble points by Monte Carlo simulation. *Molecular Physics*.

Ungerer, P., Tavitian, B., and Boutin, A.2005. *Applications of molecular simulation in the oil and gas industry: Monte Carlo methods*. Paris, France: Editions Technip.

Vega, L., Miguel, E. de, Rull, L. F. et al 1992. Phase equilibria and critical behavior of square?well fluids of variable width by Gibbs ensemble Monte Carlo simulation. *J Chem Phys* **96** (3): 2296–2305. https://doi.org/10.1063/1.462080.

Wang, C., Xiong, Y., Huang, Z. et al 2017a. *A Multi-Porosity, Multi-Physics Model to Simulate Fluid Flow in Unconventional Reservoirs*. https://doi.org/10.2118/182698-MS.

Wang, F. P. and Reed, R. M.2009. *Pore Networks and Fluid Flow in Gas Shales*. In *ATCE 2009*. Richardson, Tex.: Society of Petroleum Engineers. https://doi.org/10.2118/124253-MS.

Wang, L., Parsa, E., Gao, Y. et al 2014. *Experimental Study and Modeling of the Effect of Nanoconfinement on Hydrocarbon Phase Behavior in Unconventional Reservoirs*. https://doi.org/10.2118/169581-MS.

Wang, S., Pomerantz, A. E., Xu, W. et al 2017b. The impact of kerogen properties on shale gas production: A reservoir simulation sensitivity analysis. *Journal of Natural Gas Science and Engineering* **48**: 13–23. https://doi.org/10.1016/j.jngse.2017.06.009.

Wang, Y., Yan, B., and Killough, J.2013. *Compositional Modeling of Tight Oil Using Dynamic Nanopore Properties*. Richardson, TX. https://doi.org/10.2118/166267-MS.

Warren, J. E. and Root, P. J. 1963. *The Behavior of Naturally Fractured Reservoirs* (03): 245–255. https://doi.org/10.2118/426-PA.

Wu, Y.-S., Liu, H. H., and Bodvarsson, G. S.2004. A triple-continuum approach for modeling flow and transport processes in fractured rock. *Journal of Contaminant Hydrology* **73** (1-4): 145–179. https://doi.org/10.1016/j.jconhyd.2004.01.002.

Wu, Y.-S., Wang, C., Li, J. et al 2012. *Transient Gas Flow in Unconventional Gas Reservoir*. Society of Petroleum Engineers. https://doi.org/10.2118/154448-MS.

Xiong, Y., Winterfeld, P., Wang, C. et al 2015. Effect of Large Capillary Pressure on Fluid Flow and Transport in Stress-sensitive Tight Oil Reservoirs. In *Annual Technical Conference and Exhibition: "vibrant vision, new perspective"s, conference proceedings*, Houston, Texas, 28-30 September 2015, George R. Brown Convention Center. Richardson, Tex.: Society of Petroleum Engineers. https://doi.org/10.2118/175074-MS.

Yi Xiong. 2015. *Development of a compositional model fully coupled with geomechanics and its apllication to tight oil reservoir simulation*. Colorado School of Mines.

Zhang, Y., Lashgari, H. R., Di, Y. et al 2016. *Capillary Pressure Effect on Hydrocarbon Phase Behavior in Unconventional Reservoirs*. https://doi.org/10.2118/180235-MS.

Zuo, J. Y., Guo, X., Liu, Y. et al 2018. Impact of Capillary Pressure and Nanopore Confinement on Phase Behaviors of Shale Gas and Oil. *Energy Fuels* **32** (4): 4705–4714. https://doi.org/10.1021/acs.energyfuels.7b03975.

Zuo, Y.-X. and Stenby, E. H.1998. Prediction of Interfacial Tensions of Reservoir Crude Oil and Gas Condensate Systems. *SPE Journal* **3** (02): 134–145. https://doi.org/10.2118/38434-PA.

Appendix A

Description of molecular simulation methods

GCMC simulation

The *GCMC* ensemble is sometimes called *μVT* ensemble considers one box of simulation with constant chemical potential (μ), constant volume (V) and constant temperature (T). The z direction of the box corresponds to the slit pore of width H. This box is in thermodynamic equilibrium with a bulk reservoir of infinite number of molecules. This distribution will be sampled using acceptable trial moves. The volume of the simulation box is initially empty and different trial moves are randomly proposed and accepted or not according to the probability acceptation. These moves are generally insertion, translation, deletion and rotation of particles but longer chain molecules such as N-pentane and n-decane have internal translation and rotation in addition. At each Monte Carlo step (new configuration), number of particles inside the box are calculated. When the stationary state is reached this number of particles at each step fluctuates around its average value and then the system is at equilibrium. μVT simulation is performed at volume and temperature constant for several chemical potentials. Therefore the fluid is described from ideal gas to compressed liquid. The gap of density value in function of the fugacity allows determining the liquid/vapor equilibrium. The input fugacities values are approximated by bulk EOS calculation. More details about the GCMC simulation can be found in (Daan Frenkel and Berend Smit 1996).

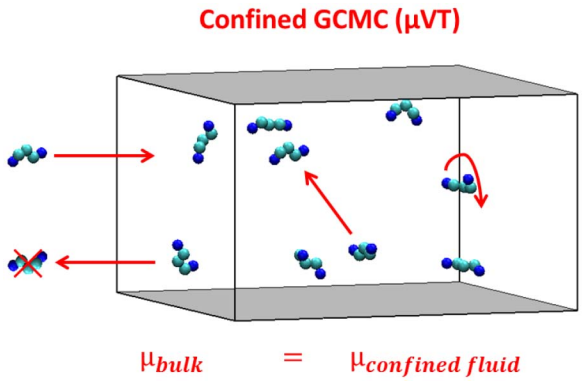

Figure 21—Schematic of the GEMC *NVT* method, example of n-pentane. Figure from Sobecki et al. (2019)

Force field parameters

Table 7—Non flexible molecule parameter

Atom	*ε(K)*	*σ(Å)*	*δ(Å)*	$\rho_s(Å^{-3})$	*M(g/mol)*
CH4	149.92	3.7372			16.043
AUA CH2	86.291	3.4612	0.38405		14.03
AUA CH3	120.15	3.6072	0.21584		15.03
Steele solid	47.0651	3.8663		0.033	

δ is the magnitude of the shift between the carbon center and the interaction site of the Anisotropic United Atom (AUA) model.

ε is the depth of the potential well.

ρ_s is the atomic density of solid.

σ is the distance between particles where inter particles potential is zero.

M is the molar mass.

Table 8—flexible molecule parameters

Bond length	$r_0(\dot{A})$	
C-C	1.535	
Bend	***θ(°)***	k_{bend} ***(K)***
CH3-CH2-CH2 CH2-CH2-CH2	114	62500
Torsion	a_i ***(K)***	
CH3-CH2-CH2-CH2 CH2-CH2-CH2-CH2	a0=1001.35 a1=2129.52 a2=-303.06 a3=-3612.27 a4=2226.71	a5=1965.93 a6=-4489.34 a7=-1736.22 a8=2817.37

θ and k_{bend} are the angle and the bending constant of the harmonic bending potential.
a_i is the constant of the torsional potential.

Appendix B

Study of pore size distributions

Pore size distribution realizations

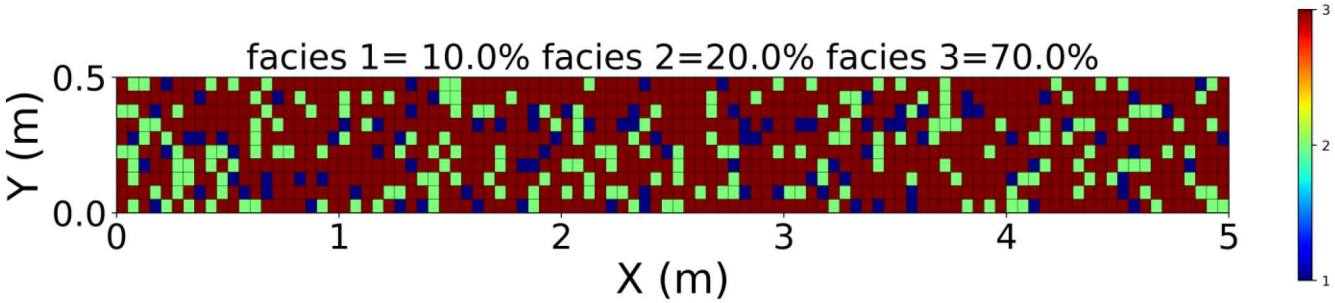

Figure 22—Example of facies distribution for distribution D1

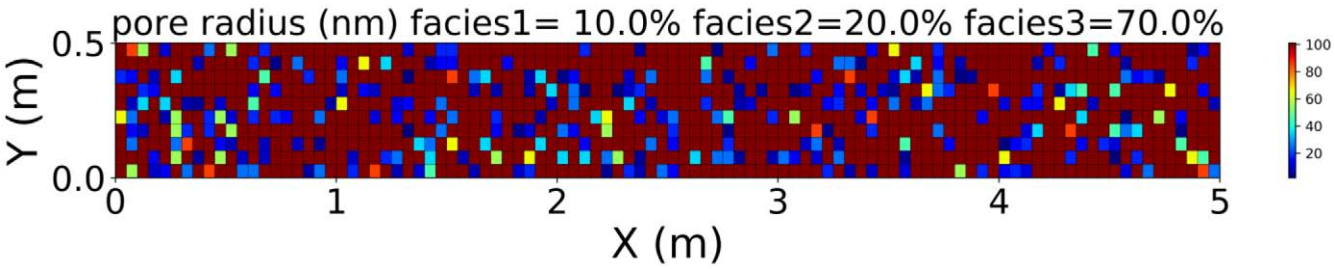

Figure 23—Example of PSD for distribution D1

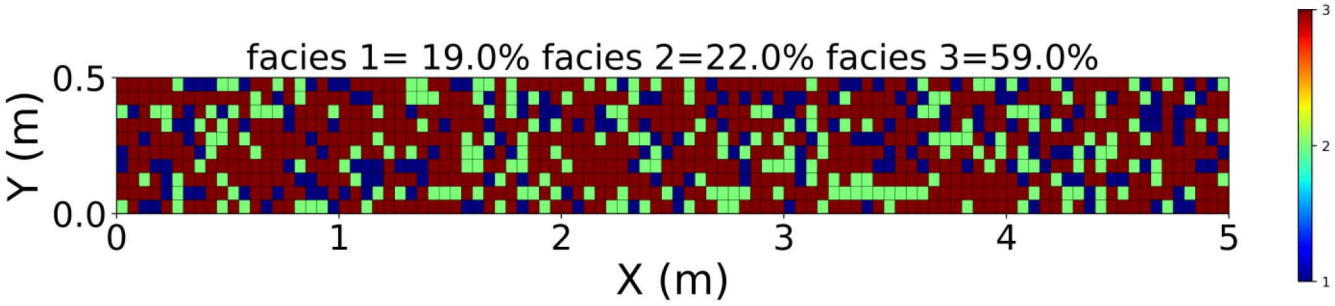

Figure 24—Example of facies distribution for distribution D2

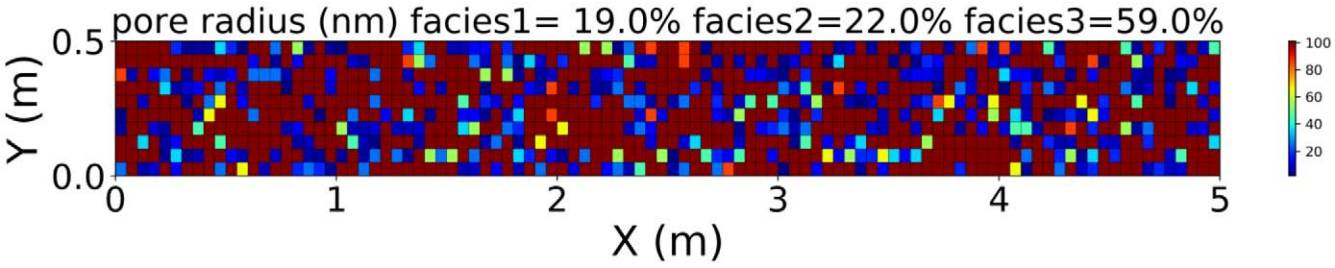

Figure 25—Example of PSD for distribution D2

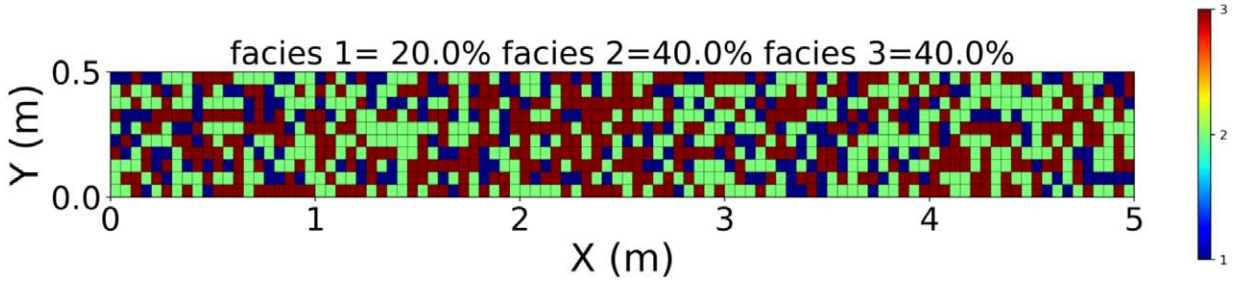

Figure 26—Example of facies distribution for distribution D3

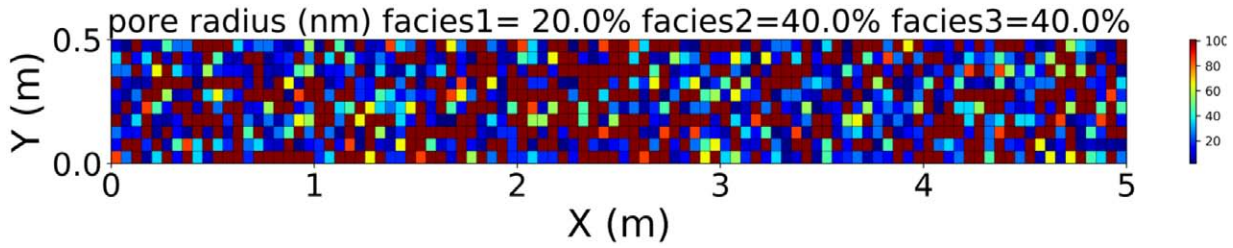

Figure 27—Example of PSD for distribution D3

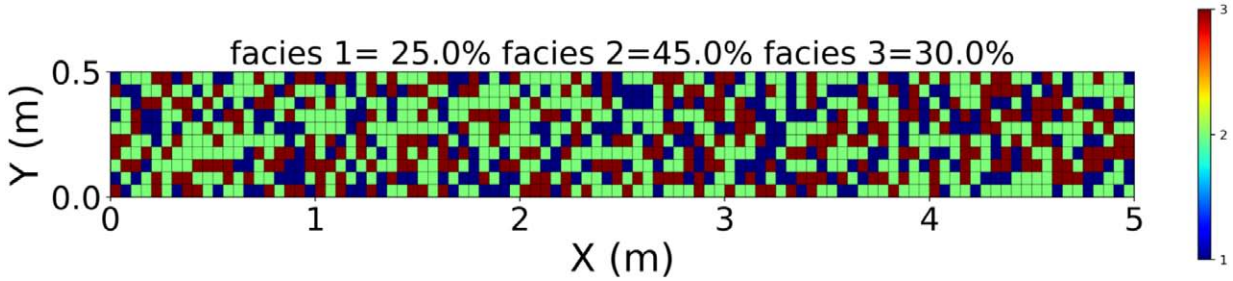

Figure 28—Example of facies distribution for distribution D4

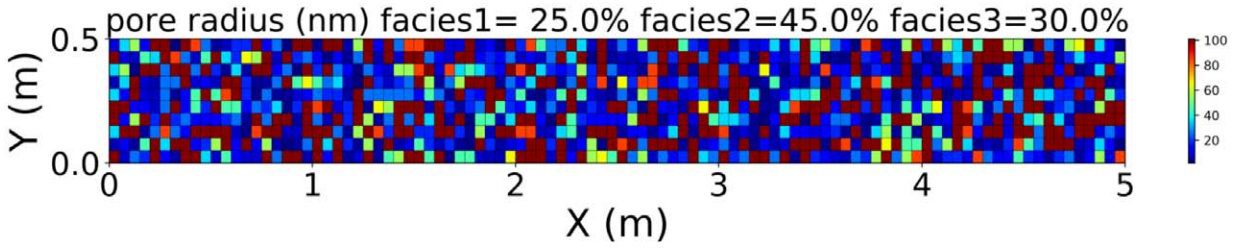

Figure 29—Example of PSD for distribution D4

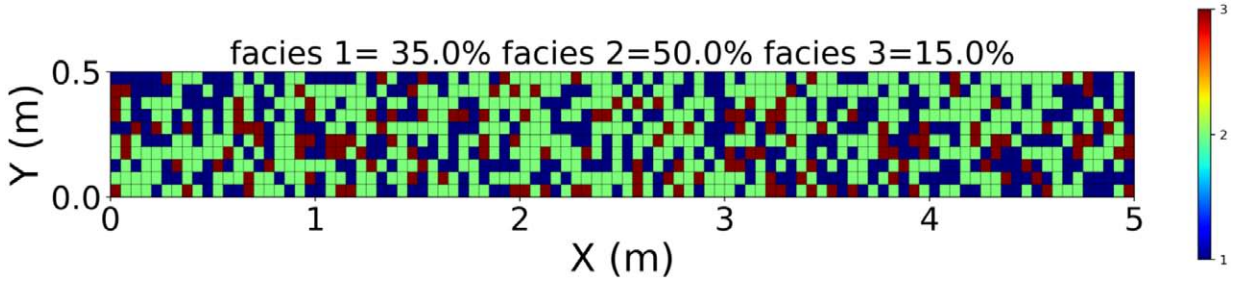

Figure 30—Example of facies distribution for distribution D5

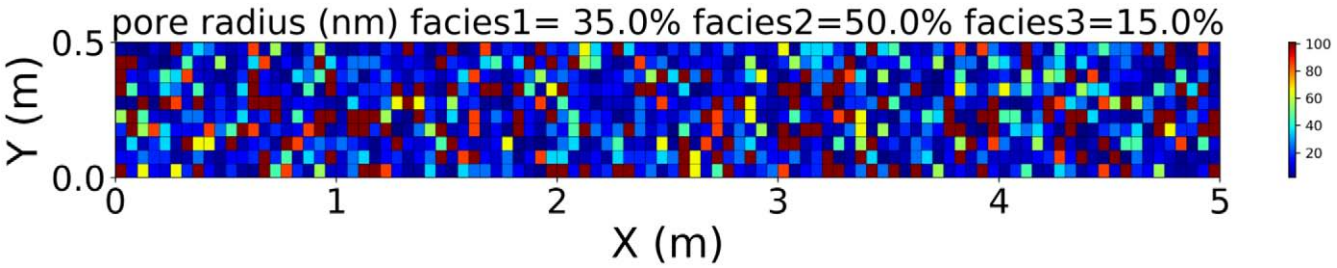

Figure 31—Example of PSD for distribution D5

Fine grid simulation results

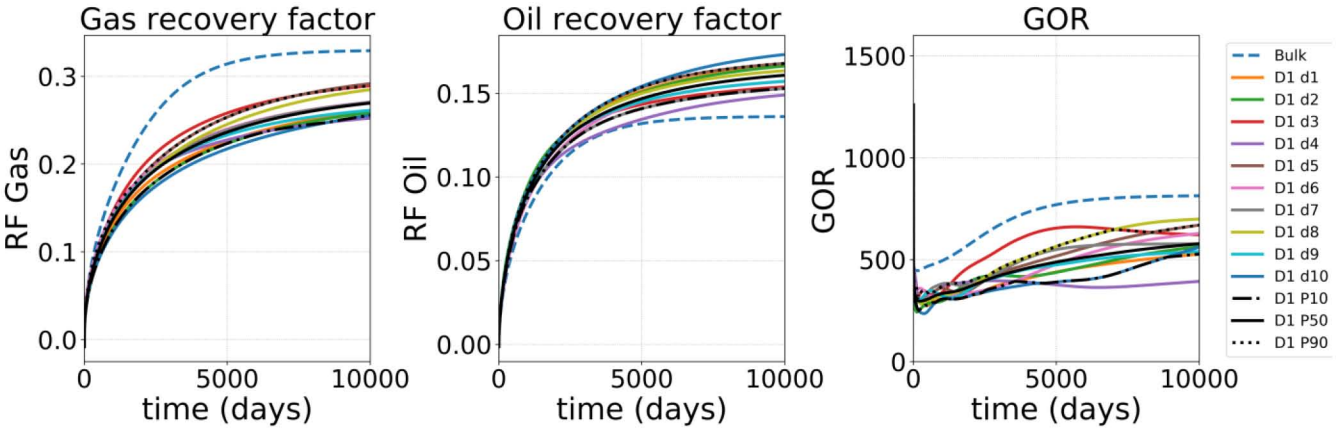

Figure 32—Production results for the ten samples of distribution D1 compared to bulk

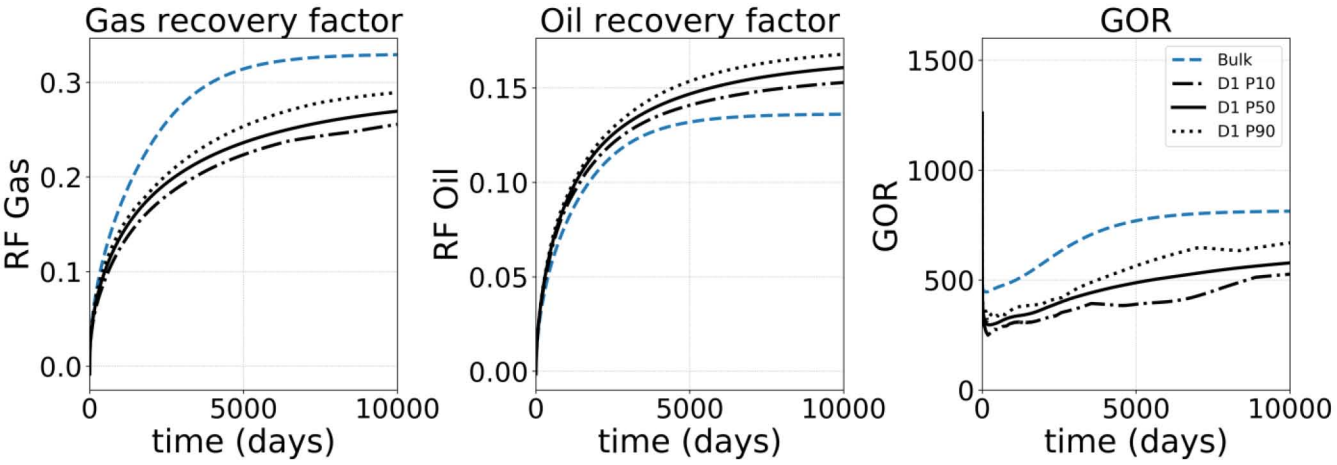

Figure 33—Production results of distribution D1 compared to bulk

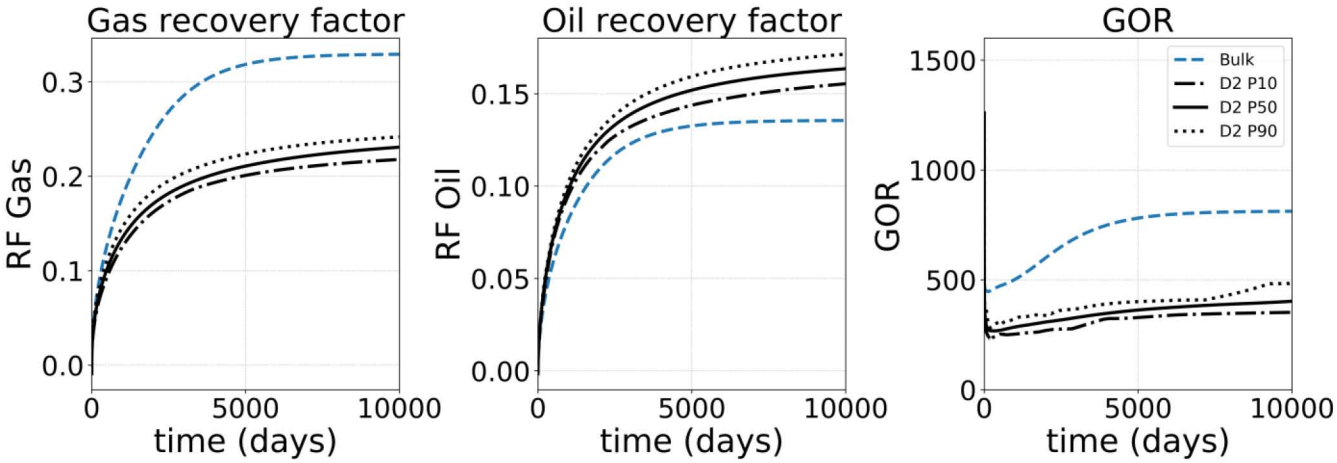

Figure 34—Production results of distribution D2 compared to bulk

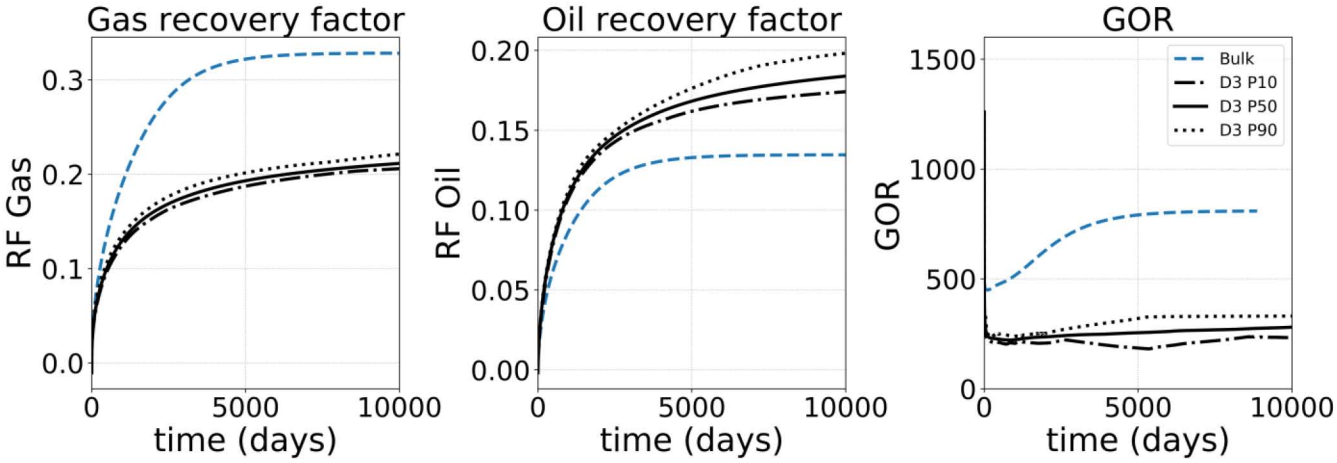

Figure 35—Production results of distribution D3 compared to bulk

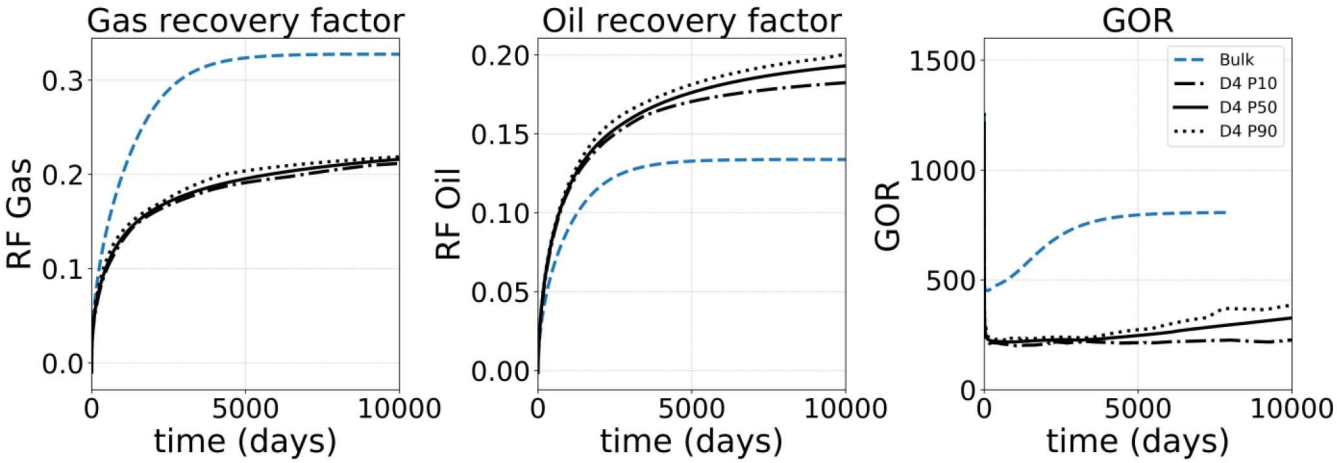

Figure 36—Production results of distribution D4 compared to bulk

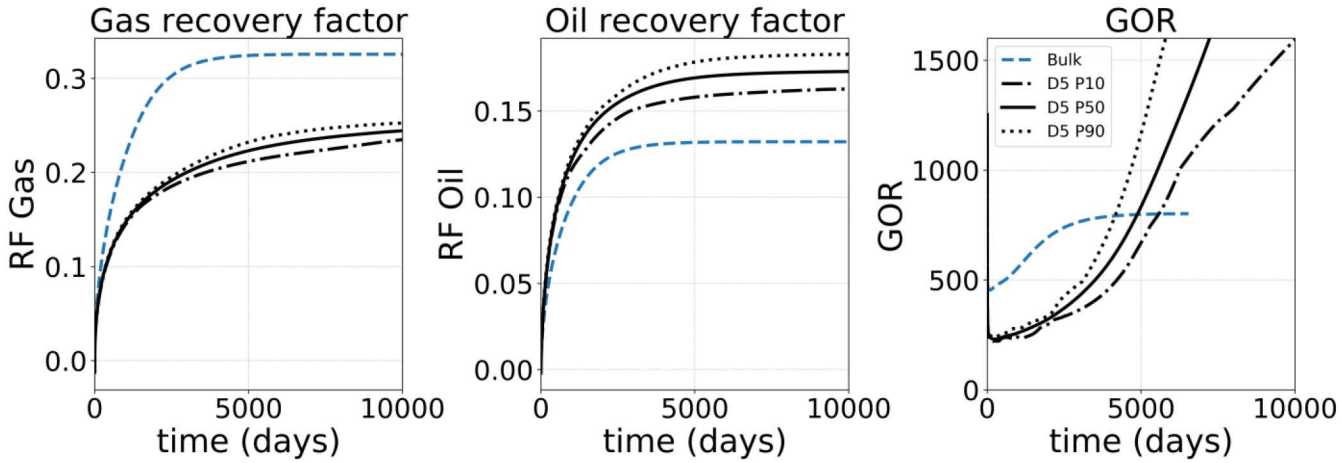

Figure 37—Production results of distribution D5 compared to bulk

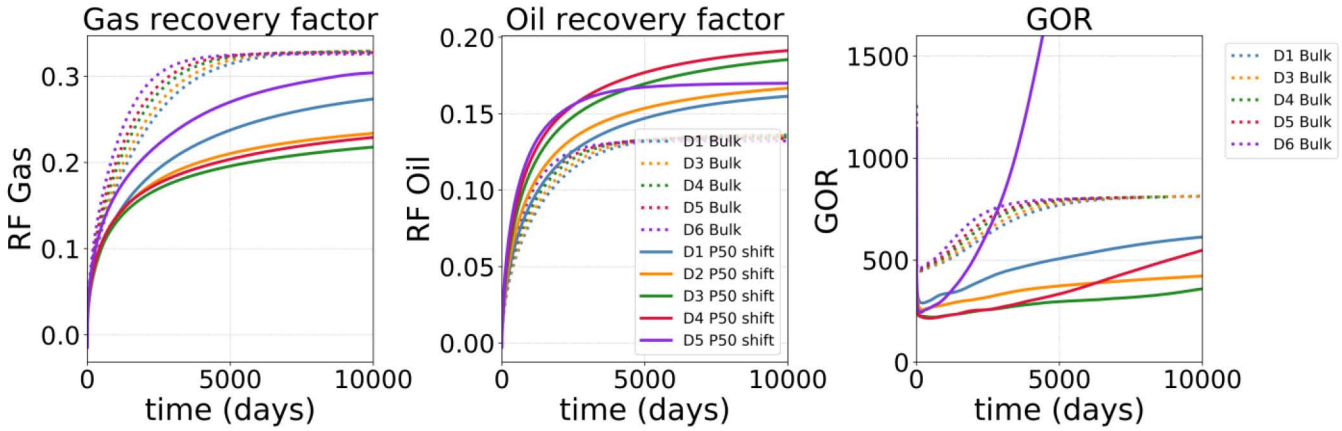

Figure 38—Comparison of production results for the different distributions with a flash with critical point shift

Coarse grid simulations

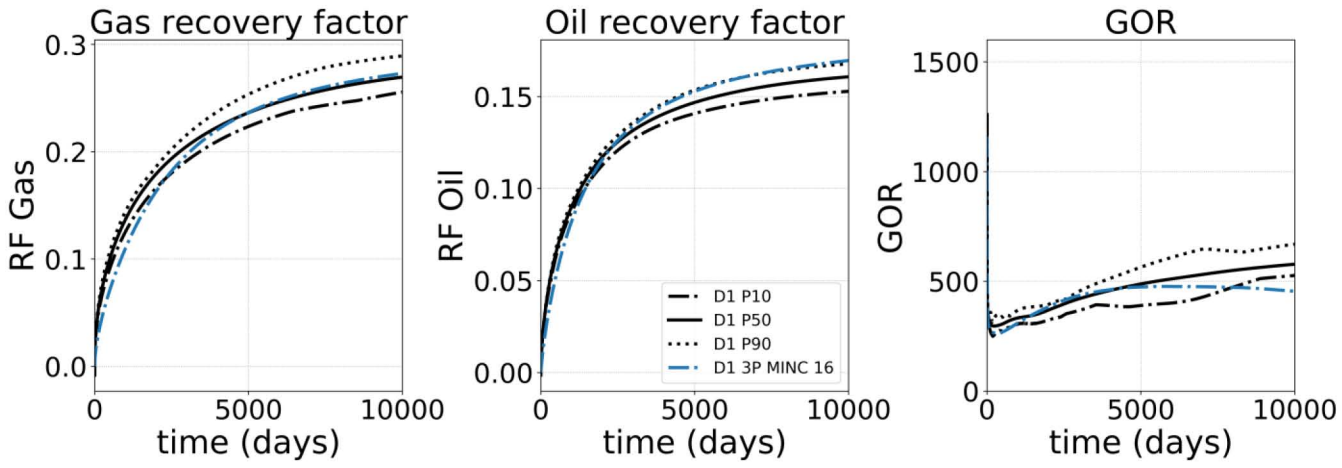

Figure 39—3P matching for D1

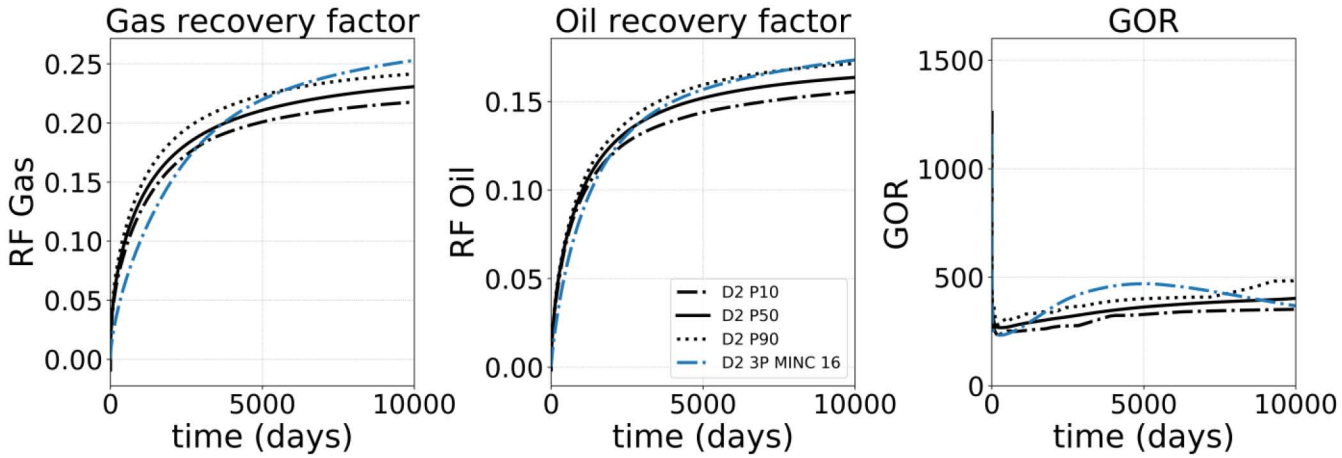

Figure 40—3P matching for D2

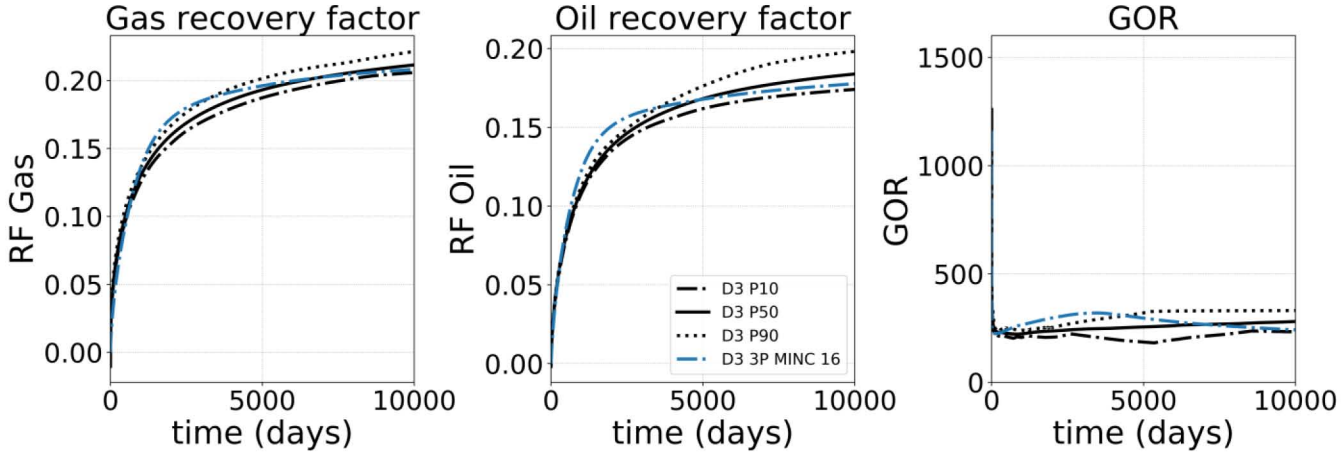

Figure 41—3P matching for D3

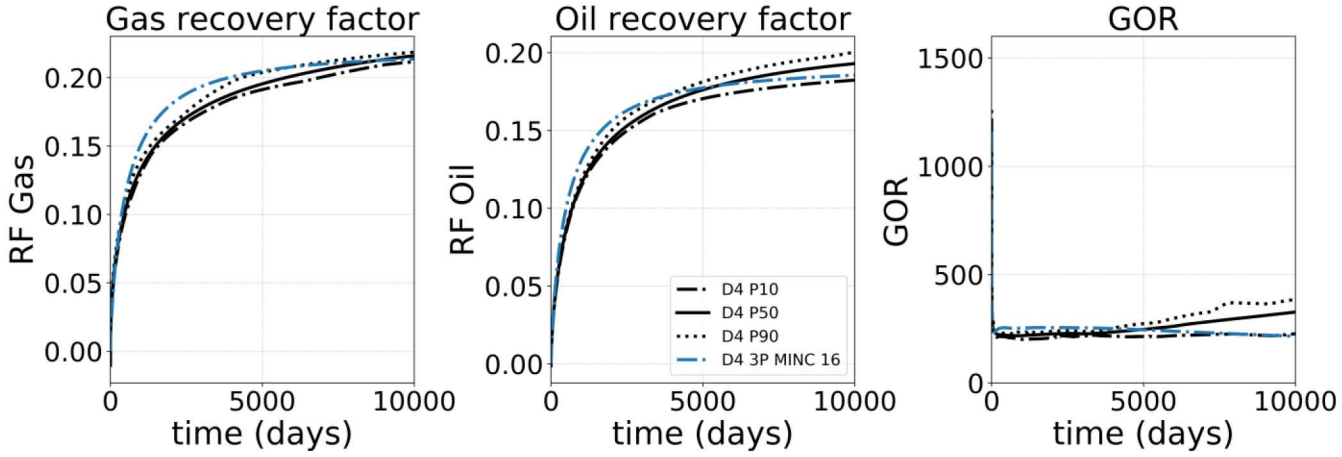

Figure 42—3P matching for D4

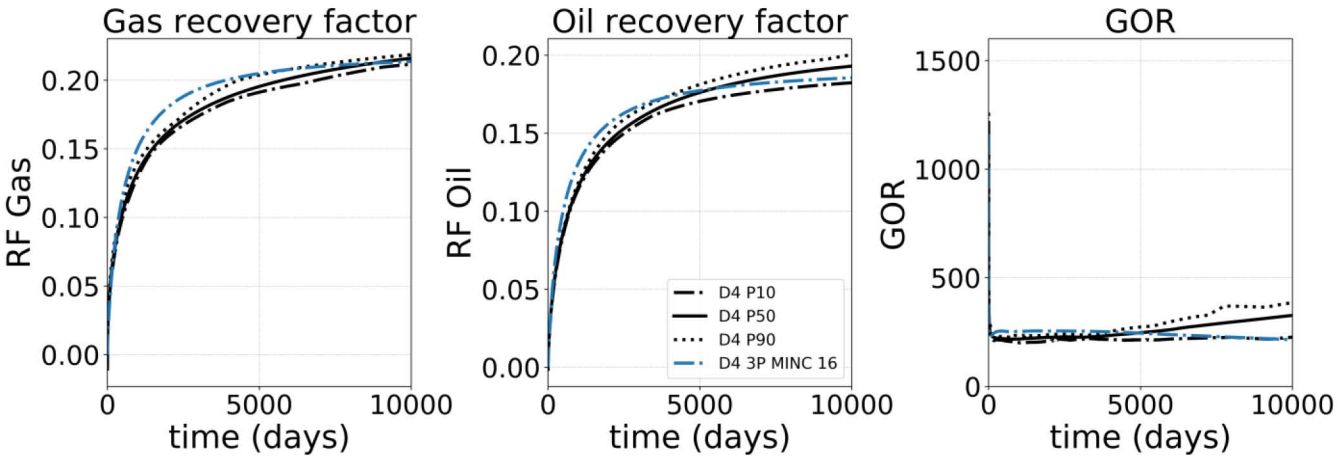

Figure 43—3P matching for D5